

Identifying Host Galaxies of Binary Black Hole Mergers with Next-Generation Gravitational Wave Detector Networks

Sumedha Biswas¹  , Andrew Levan^{1,2}, Peter G. Jonker¹ , Kendall Ackley² , Gregory Ashton³ , Nikhil Sarin^{4,5} 

¹ Department of Astrophysics/IMAPP, Radboud University, PO Box 9010, 6500 GL Nijmegen, The Netherlands

² Department of Physics, University of Warwick, Coventry, CV4 7AL, UK

³ Department of Physics, Royal Holloway University of London, Egham, TW20 0EX

⁴ Kavli Institute for Cosmology, University of Cambridge, Madingley Road, CB3 0HA, UK

⁵ Institute of Astronomy, University of Cambridge, Madingley Road, CB3 0HA, UK

arXiv:2602.08459v1 [astro-ph.HE] 9 Feb 2026

Accepted XXX. Received YYY; in original form ZZZ

ABSTRACT

Identifying the host galaxy of a binary black hole (BBH) merger detected via gravitational waves (GWs) remains a challenge due to the absence of electromagnetic counterparts and the large localization volumes produced by current-generation detectors. A confident host association would provide stellar population properties to constrain BBH formation channels and enable measurements of cosmological parameters such as the Hubble constant, H_0 . We simulate BBH mergers in nearby ($z < 0.25$) host galaxies to evaluate the feasibility of host identification with future GW detector networks, including configurations with the planned LIGO-India detector and third-generation detectors such as the Einstein Telescope (ET) and Cosmic Explorer (CE). We construct two injection grids to explore variations in BBH mass, distance, and directional sensitivity, and infer localization volumes using the Fisher Information Matrix (FIM)-based parameter estimation implemented through BILBY. To assess the prospects for unique host identification, we introduce a set of diagnostics: theoretical comoving volume thresholds for galaxies of a given stellar mass, derived from galaxy stellar mass functions (GSMFs), a metallicity-based volume threshold motivated by progenitor environment models, stellar mass fractions to quantify candidate host prominence, and the probability of chance alignment (p_c). These metrics provide ways to evaluate host associations and constrain BBH formation channels. We find that future networks that include ET and CE localize BBH mergers to volumes smaller than those theoretical thresholds, implying potentially unique host identification, out to ~ 1000 Mpc at a rate of ~ 100 yr⁻¹. While associations for individual events may remain uncertain, our framework is well-suited to population-level analyses, enabling constraints on BBH formation scenarios in the era of next-generation GW detector networks.

Key words: gravitational waves – black hole physics – galaxies: statistics

1 INTRODUCTION

The discovery of gravitational waves (GW) from a binary black hole (BBH) merger was made during the first observing run (O1) of the two LIGO detectors at Hanford and Livingston (USA) in 2015, marking the beginning of GW astrophysics (Abbott et al. 2016). Since then, the two LIGO detectors have undergone further upgrades in sensitivity (Abbott et al. 2018; Capote et al. 2025; Abac et al. 2025b), and Advanced Virgo (Acernese et al. 2014, 2019, 2023) in Italy and KAGRA (Aso et al. 2013; Kagra Collaboration et al. 2019; Akutsu et al. 2020) in Japan have been operational, since 2017 and 2020, respectively. With this combined GW detector network, many BBH mergers and other compact binary coalescences (CBCs) have been detected across successive observing runs. Combining data from the GW transient catalogues (GWTC-1.0: Abbott et al. 2019, GWTC-2.0, 2.1: Abbott et al. 2021a, 2024, GWTC-3.0: Abbott et al.

2023b, and GWTC-4.0: Abac et al. 2025c), there are 218¹ GW event candidates in total, comprising 210 BBH mergers, 2 binary neutron star (BNS) mergers, and 6 neutron star–black hole (NSBH) mergers.

GW transients, involving at least one neutron star (NS), i.e. BNS and NSBH mergers, can produce a range of electromagnetic (EM) counterparts such as gamma-ray bursts (e.g. Eichler et al. 1989), kilonovae (e.g. Li & Paczyński 1998a; Metzger & Berger 2012; Tanvir et al. 2013; Coulter et al. 2017; Smartt et al. 2017a; Rastinejad et al. 2022; Troja et al. 2022; Levan et al. 2024), and potentially fast X-ray transients (e.g. Siegel & Cioffi 2016a; Siegel & Cioffi 2016b; Sun et al. 2017, 2019; Sun et al. 2024; Quiróla-Vásquez et al. 2024; Biswas et al. 2025). These signatures are thought to arise from the accretion of a remnant disk onto the massive NS or BH remnant following the merger (e.g. Narayan et al. 1992), radioactive decay of heavy, neutron-rich, elements synthesised through the *r*-process

* E-mail:s.biswas@astro.ru.nl

¹ GW candidates with a probability of astrophysical origin $p_{\text{astro}} \geq 0.5$;

in the expanding merger ejecta (Li & Paczyński 1998b; Tanvir et al. 2017a), or the spin-down energy of a millisecond magnetar (e.g. Lin et al. 2022). In the case of NSBH mergers, the outcome depends on the binary parameters (e.g. Davies et al. 2005; Foucart et al. 2013): the NS may be tidally disrupted outside the event horizon of the BH, leading to substantial mass ejection, or it may plunge directly into the BH with little or no ejecta. Since their GW signals are typically louder than those of BNS mergers, and tidal disruption can eject more material, giving rise to brighter kilonovae, NSBH mergers are regarded as especially promising targets for EM follow-up (Gupta et al. 2023). During O3, two NSBH mergers (Abbott et al. 2021b) were detected; however, neither yielded an EM counterpart. In contrast, BBH mergers, are generally not expected to produce EM emission, although possible EM bright scenarios do exist, for example if the merger occurs in a gas-rich environment such as the accretion disks of active galactic nuclei (AGN) (e.g. Perna et al. 2016; McKernan et al. 2019; Graham et al. 2020). Notably, the first detected BBH merger, GW150914 (Abbott et al. 2016), was temporally and spatially coincident with a weak gamma-ray burst detected by *Fermi*-GBM (Ackermann et al. 2016; Connaughton et al. 2016) although no optical or radio emission was detected (Savchenko et al. 2016), and this association remains debated (e.g. Janiuk et al. 2017; Connaughton et al. 2018). In another BBH merger, GW190521 (Abbott et al. 2020b), a contemporaneous optical flare lasting several months from an active galactic nucleus within the GW localization volume was found, with Graham et al. (2020) suggesting the possibility of it occurring inside the accretion disk of a central supermassive BH. However, these claims remain controversial, and are not generally accepted at the present time (e.g. Palmese et al. 2021; Veronesi et al. 2025). Hence, at present there are no clear EM counterparts, or indeed precise localizations and host galaxy associations, for any BBH mergers.

One of the primary challenges in GW astronomy is the precise localization of CBCs, as GW skymaps often span up to hundreds or thousands of square degrees on the sky (Gehrels et al. 2016; Abbott et al. 2020a; Pankow et al. 2020). The identification of an EM counterpart significantly improves the localization, as demonstrated in the case of GW170817 (Abbott et al. 2017), a BNS merger that occurred at a nearby distance of 40 Mpc and was associated with a range of EM counterparts across the spectrum (Andreoni et al. 2017; Arcavi et al. 2017; Chornock et al. 2017; Coulter et al. 2017; Covino et al. 2017; Cowperthwaite et al. 2017; Drout et al. 2017; Kasliwal et al. 2017; Evans et al. 2017; Lipunov et al. 2017; Nicholl et al. 2017; Pian et al. 2017; Shappee et al. 2017; Smartt et al. 2017b; Tanvir et al. 2017b; Troja et al. 2017; Yang et al. 2019; Utsumi et al. 2017; Soares-Santos et al. 2017), and was subsequently successfully associated with its host, NGC 4993 (Levan et al. 2017; Im et al. 2017; Ebrová et al. 2020; Kilpatrick et al. 2022). Conversely, in the case of BBH mergers, which are generally assumed to have no associated EM counterparts, GW localization and host identification become extremely challenging since they must be undertaken purely on the basis of GW information. However, it is astrophysically important. The properties of the BBH environment play a critical role in constraining both formation and merger pathways (see Mapelli 2020 for a detailed review). For instance, low-metallicity environments may favour the formation of more massive stellar-origin BBHs (e.g. Lamberts et al. 2016), while dense stellar regions such as globular clusters may support hierarchical BH assembly through repeated dynamical interactions (e.g. Antonini et al. 2019; Martinez et al. 2020; Ye et al. 2022). A uniquely identified host galaxy (or even location within the host galaxy) provides direct measurements of the underlying stellar population properties such as total stellar mass, age of the dominant

population and metallicity that can be directly compared to the predictions of different formation channels. Beyond constraining these channels, host identification also has cosmological applications; for instance, it provides a method for an independent redshift measurement to be combined with the luminosity distance inferred from GW observations, enabling a direct measurement of the Hubble constant (e.g. Abac et al. 2025d). Since BBH mergers can be found at much larger distances than those containing NSs, they probe well into the Hubble flow and can, therefore, enable better constraints on expansion histories with fewer observations by, for example, minimising uncertainties due to peculiar motions that were substantial in the case of GW170817 (Hjorth et al. 2017; Cantiello et al. 2018). In the absence of host identification, several studies have utilized BBH mergers as statistical dark sirens to place constraints on the Hubble constant (e.g. MacLeod & Hogan 2008; Del Pozzo 2012; Gray et al. 2022; Bom et al. 2024; Ghosh et al. 2024), but even a small number of unique host identifications would provide great diagnostic power.

Although localizing BBH mergers remains challenging with current detector sensitivities, it may be possible in some circumstances (Nuttall & Sutton 2010; Chen & Holz 2016; Howell et al. 2018), and this limitation may not persist in the coming decades. By the mid-2030s, a range of developments is expected to dramatically improve GW sky localization. Future detections of stellar-mass BBH mergers may be preceded by months to years of inspiral signals in the millihertz regime (Ewing et al. 2021), detectable by the space-based Laser Interferometer Space Antenna (LISA) detector (Amaro-Seoane et al. 2017; Colpi et al. 2024), allowing advanced pre-merger localization. On the ground, localization prospects will improve with the planned addition of LIGO-India (Unnikrishnan 2013, 2023; Shukla et al. 2024) to the existing network of advanced detectors. Crucially, third-generation (3G) detectors such as the Einstein Telescope (ET) (Punturo et al. 2010; Hild et al. 2011; Maggiore et al. 2020; Abac et al. 2025a) and Cosmic Explorer (CE) (Reitze et al. 2019; Evans et al. 2021, 2023) are predicted to have an order-of-magnitude improvement in sensitivity (Borhanian & Sathyaprakash 2024). When operating in conjunction with 2G detectors, these facilities will potentially enable precise 3D localization for nearby, high signal-to-noise ratio (SNR) BBH events, achieving sky areas $< 1 \text{ deg}^2$ (Borhanian & Sathyaprakash 2024; Gupta et al. 2024a; Mo & Chen 2024).

In this paper, we investigate the feasibility of identifying hosts of BBH mergers using future GW detector networks. We simulate BBH mergers injected into M_* galaxies and construct two complementary injection grids, Grids I and II, to explore how localization performance depends on source properties (mass and distance) and directional sensitivity (Section 2.2). We first define three GW detector network configurations: HLV, HLVKIEC, and EC (Section 2.1); and then perform parameter estimation using the Fisher Information Matrix (FIM) formalism implemented in BILBY (Section 2.3). The resulting posteriors are used to compute 3D localization volumes for each injection (Section 2.4). We then compare these volumes to theoretical comoving volume thresholds derived from galaxy stellar mass functions, including versions weighted by assumptions about isolated and dynamical BBH formation scenarios (Section 2.5). To further assess the astrophysical utility of these volumes, we introduce a set of diagnostics: a metallicity-based threshold (Section 2.6.1), mass fractions (Section 3.1.3), and probability of chance alignment (Section 3.2). In Section 4, we present detailed analyses of localization performance across both injection grids, using each of the proposed diagnostics. These analyses are used to compare detector network performance (Section 5.1) and to evaluate the extent to which hosts may be identified and BBH formation channels statistically constrained (Section 5.2). We summarize our findings and

discuss future directions in Section 6. In Appendix A, we explore how our assumptions about GW source parameters influence the analysis outcomes and compare our adopted values to those inferred from observed GW events.

2 METHODS

We adopt a flat Λ CDM cosmology with a matter density parameter $\Omega_m = 0.3$ throughout this analysis. For sections of the study requiring observed galaxy information, we use the NED Local Volume Sample (NED-LVS; Cook et al. 2023), a subset of ~ 2 million objects in NED with distances out to 1000 Mpc. For bright galaxies ($\geq L^*$), NED-LVS is $\sim 100\%$ complete out to ~ 400 Mpc (Cook et al. 2023). The catalogue adopts $H_0 = 69.6 \text{ km s}^{-1} \text{ Mpc}^{-1}$, which we also use in relevant calculations to ensure consistency.

2.1 GW Detector Networks

We consider the following GW detectors in our analysis: *current-generation detectors*—LIGO-Hanford (H), LIGO-Livingston (L) (Abbott et al. 2009), Virgo (V) (Acernese et al. 2014), and KAGRA (K) (Kagra Collaboration et al. 2019); and *proposed third-generation detectors*—Einstein Telescope (E) (Punturo et al. 2010; Hild et al. 2011; Maggiore et al. 2020; Abac et al. 2025a), Cosmic Explorer (C) (Reitze et al. 2019; Evans et al. 2021, 2023), and LIGO-India (I) (Unnikrishnan 2013, 2023; Shukla et al. 2024). The specifications of each detector, such as the location, frequency range, and orientation, are listed in Table 1. Based on these, we define three GW detector networks that we use throughout this study: HLVKIEC, HLV, and EC. For each detector, we use publicly available power spectral density (PSD) data².

2.2 Injection Grids

With the detector networks established, we proceed to construct two complementary grids of GW injections to evaluate how both sky location and detector sensitivity affect localization performance.

(i) **Grid I:** We select 3 M_* galaxies—systems with typical total stellar masses near the characteristic “knee” of the double Schechter galaxy stellar mass function (Equation 1), marking the transition from the abundant low-mass population to the rarer massive galaxies—from the NED-LVS galaxy catalogue, located at distances of ~ 500 Mpc, ~ 750 Mpc, and ~ 1000 Mpc respectively (Table 2). These distances are similar to several of the BBH detections reported in GWTC 4.0 (Abbott et al. 2019, 2021a, 2024, 2023b; Abac et al. 2025c) and are sufficiently close that well-constrained skymaps maintain reasonably small comoving volume regions that can be realistically surveyed for galaxies with existing telescopes. In each galaxy, we simulate a BBH merger with one of the following component mass configurations: $50+50 \text{ M}_\odot$, $40+40 \text{ M}_\odot$, $30+30 \text{ M}_\odot$, $20+20 \text{ M}_\odot$, $10+10 \text{ M}_\odot$, and $5+5 \text{ M}_\odot$. This results in an injection grid with a total dimension of $3 \times 3 \times 6$ for 3 GW detector networks.

(ii) **Grid II:** To explore the “best” and “worst” case scenarios for detector network performance and compare the performance of the HLVKIEC and EC detector networks, we incorporate directional sensitivity using the network antenna patterns. The response of a GW detector to a signal depends on its antenna pattern functions F_+ and

F_\times , which quantify the sensitivity of the detector to the two independent polarization states of a GW signal (Finn 2001; Schutz 2011). To construct this grid, we select arbitrary sky locations within the most sensitive (“bright”) and least sensitive (“dark”) regions of each detector network’s (HLVKIEC and EC) antenna pattern (Figure 2, Table 3). At each of these positions, we simulate BBH mergers at the same three distances and BBH mass configurations as in Grid I. This results in an injection grid with a total dimension of $2 \times 2 \times 3 \times 6$ for 2 GW detector networks. We exclude the HLV network from Grid II as the FIM-based parameter estimation (PE; discussed in Section 2.3) becomes unreliable due to low SNRs.

2.3 Parameter Estimation with BILBY

To perform PE on our simulated GW injection grid, we use the Bayesian inference library BILBY (Ashton et al. 2019). All analyses are performed using the `IMRPhenomXPHM` waveform approximant (Pratten et al. 2021), a frequency-domain, precessing, phenomenological model well-suited to modeling the inspiral, merger, and ring-down of non-eccentric BBHs. For each injection, we use Grid I or Grid II values (Section 2.2, Tables 2, 3), while keeping all other parameters fixed across runs (Table 4). PE is performed using standard astrophysical priors (Table 5): we assume uniform priors on Right Ascension (RA), polarization angle ψ , and coalescence phase ϕ_c ; sinusoidal priors on the inclination angle θ_{JN} ; and a cosine prior on Declination (Dec). The luminosity distance prior d_L between 1 and 10000 Mpc, is uniform in comoving volume and source frame time i.e. $\propto \frac{1}{1+z} \frac{dV_c}{dz}$ where V_c is the comoving volume. The coalescence time is allowed to vary within a ± 0.5 s window around the injection time. All other parameters, including masses and spins, are fixed to their injected values.

Given the extremely high signal-to-noise ratios (Figure 1) and the long signal durations in some of our low-mass injections, nested samplers such as `dynesty` (Speagle 2020) or `nestle` face computational challenges in efficiently exploring the resulting sharply peaked posterior distributions. We therefore adopt the Fisher Information Matrix (FIM) approximation (Vallisneri 2008), which approximates the log-likelihood around the maximum-likelihood point to produce an analytic Gaussian approximation to the posterior. This method is well-justified in the high-SNR limit. From this, we generate posterior samples that can be used to construct credible regions.

2.4 Localization Volumes

For each simulated GW event, we compute the 3D localization volume by combining the sky localization area with luminosity distance constraints derived from the FIM-based posterior distributions. We begin by extracting the posterior samples for RA, Dec, and luminosity distance d_L . To estimate the sky localization area, we apply a 2D kernel density estimate (KDE) (Rosenblatt 1956; Parzen 1962) to the RA and Dec samples, evaluate the density on a HEALPix grid (Górski et al. 2005) with resolution parameter `nside` = 2048, and identify the smallest set of pixels enclosing 50% and 90% of the posterior probability. Figure A1 shows an example of the 2D localization areas of a $50 \text{ M}_\odot + 50 \text{ M}_\odot$ injection at 1000 Mpc. We extract the central credible interval from the d_L posterior distribution, convert the lower and upper bounds to redshift using the assumed cosmology, and compute the comoving shell volume between z_{min} and z_{max} . The final 3D localization volume is obtained by multiplying this shell volume by the fractional solid angle subtended by the sky localiza-

² Design Sensitivity curves have been downloaded from: [LIGO-T2000012-v2](https://ligo-t2000012-v2.ce-T2000017-v8), [CE-T2000017-v8](https://ligo-t2000017-v8), and [ET](https://ligo-t2000017-v8)

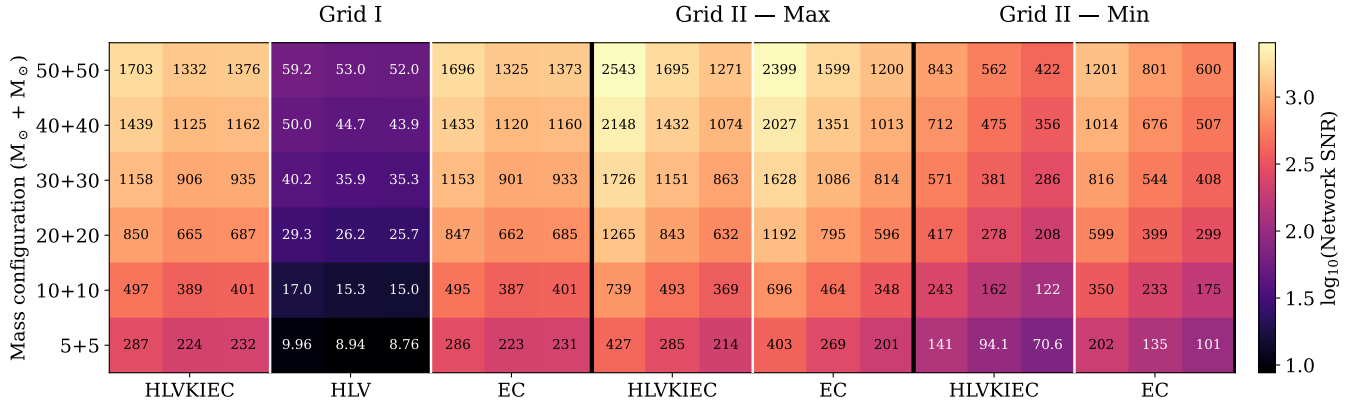


Figure 1. Heatmap of the network optimal SNRs for the injected BBH mergers across masses and distances. *Black* vertical lines separate Grids I and II (maximum and minimum sensitivity), and the *white* vertical lines separate the GW detector networks. Each triplet of columns within a network corresponds to distances of 500, 750, and 1000 Mpc (*left to right*), and rows correspond to mass configurations from $50+50 M_\odot$ (*top*) to $5+5 M_\odot$ (*bottom*). The colourbar indicates the logarithm of the network optimal SNR, with lighter shades corresponding to higher SNR values. The network optimal SNR is calculated as $\rho_{\text{network}} = \sqrt{\sum_j \rho_j^2}$, where ρ_j is the optimal matched-filter SNR in detector j .

Table 1. GW detector network specifications.

Detector	Location (Lat, Lon)	Frequency Range (Hz)	Arms	Orientation (Azimuths)
LIGO Hanford (H)	46.45°N, 119.41°W	20–2000	2	36.8°, 126.8°
LIGO Livingston (L)	30.56°N, 90.77°W	20–2000	2	108.0°, 198.0°
Virgo (V)	43.63°N, 10.50°E	20–2000	2	19.4°, 109.4°
KAGRA (K)	36.41°N, 137.30°E	20–2000	2	25°, 295°
LIGO-India (I)	19.61°N, 77.02°E	20–2000	2	TBD
Einstein Telescope (ET)	50.85°N, 5.70°E	1–10,000	3	0°, 120°, 240°
Cosmic Explorer (CE)	46.45°N/30.56°N, 119.41°W/90.77°W	5–5,000	2	Site-dependent

Notes: Orientation angles are azimuths measured clockwise from geographic north. L-shaped detectors have 90° arm separations. ET is planned to have three 10 km arms arranged in an equilateral triangle. CE's final orientation depends on site selection (40 km arms). Frequency ranges represent approximate design goals.

Table 2. Properties of the injected M_* hosts in Grid I, selected from the NED-LVS galaxy catalogue. For each injection distance, the corresponding characteristic stellar mass M_* was determined using the corresponding Schechter function parameters (see Table 6).

Galaxy Name	RA, Dec [deg]	Distance [Mpc]	Redshift	Stellar Mass [M_\odot]
WISEA J171543.62+291712.7	258.93177, 29.28687	499.922 ± 0.145	0.12	$6.16 \times 10^{10} M_\odot$
WISEA J142633.23+335512.5	216.63848, 33.92015	750.081 ± 0.053	0.18	$6.15 \times 10^{10} M_\odot$
WISEA J205335.01+010024.3	313.39591, 1.00678	999.938 ± 0.326	0.23	$4.93 \times 10^{10} M_\odot$

tion region. The 50% (V_{50}) and 90% (V_{90}) localization volumes are then used for further analyses.

2.5 Galaxy Mass Weighting Across BBH Formation Channels

Several formation channels have been proposed for BBHs (see Mapelli 2020 for a detailed review): BBH mergers can be the result of isolated binary evolution via common envelope (Bethe & Brown 1998; Portegies Zwart & Yungelson 1998; Belczynski et al. 2002, 2008; Belczynski et al. 2016; Dvorkin et al. 2016; Dvorkin et al. 2018; Eldridge & Stanway 2016; Mapelli et al. 2017; Mapelli et al. 2019; Stevenson et al. 2017; Kruckow et al. 2018; Spera et al. 2019; Belczynski, K. et al. 2020; Klencki, Jakub et al. 2021; Olejak et al. 2021; Tanikawa et al. 2021), stable mass transfer (Giacobbo et al. 2018; Neijssel et al. 2019; Bavera et al. 2021; Gallegos-Garcia

et al. 2021; Shao & Li 2021), or chemically homogeneous evolution (de Mink & Mandel 2016; Mandel & de Mink 2016; Marchant et al. 2016; du Buisson et al. 2020; Riley et al. 2021). Alternatively, BBHs can form dynamically in triples (e.g. Antonini et al. 2017; Silsbee & Tremaine 2017; Arca Sedda, Manuel et al. 2021), multiples (e.g. Fragione & Kocsis 2019; Hamers & Safarzadeh 2020), young stellar clusters (e.g. Banerjee et al. 2010; Mapelli 2016; Banerjee 2017; Kumamoto et al. 2020), globular clusters (GCs) (Portegies Zwart & McMillan 2000; Tanikawa 2013; Samsing et al. 2014; Rodriguez et al. 2016; Askar et al. 2017; Fragione & Kocsis 2018; Hong et al. 2018; Choksi et al. 2019), and nuclear star clusters (e.g. Arca Sedda et al. 2020; Fragione et al. 2020).

These disparate formation channels may result in markedly different formation environments; however, the delay time between the formation and merger also means that the formation environment and

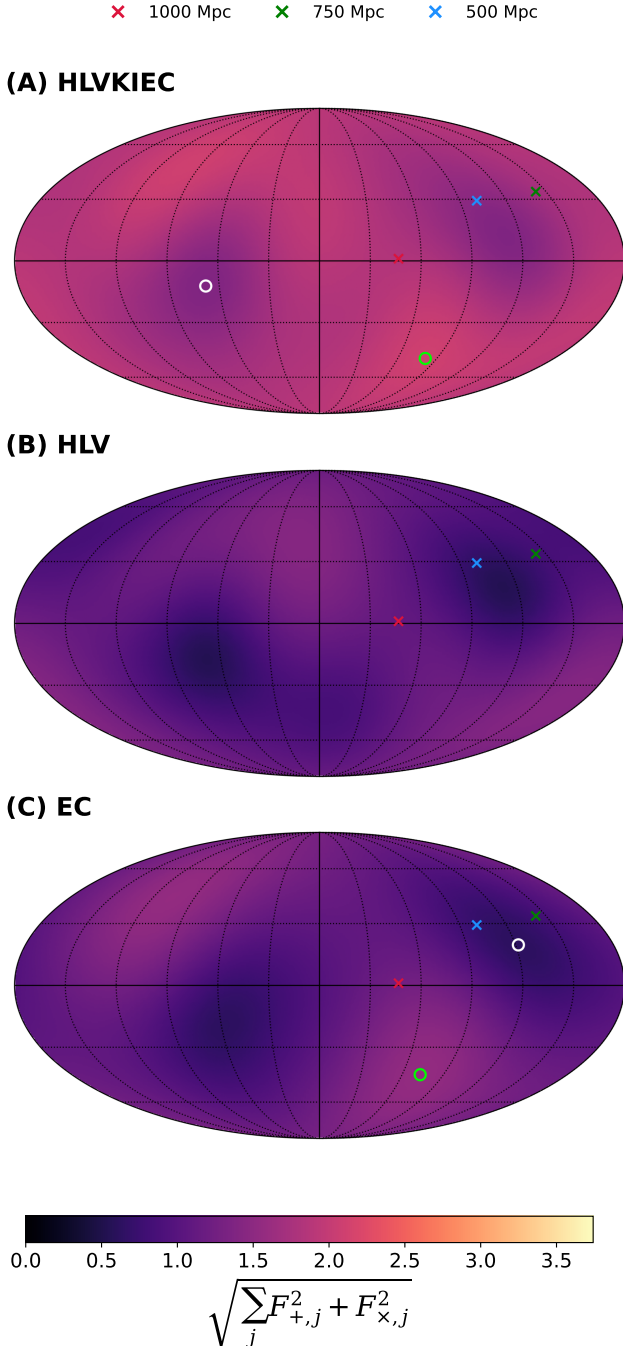


Figure 2. Antennae pattern maps for the three GW detector networks considered in this study: (A) HLVKIEC, (B) HLV, and (C) EC. Each panel shows the combined network antenna amplitude response, defined as $\sqrt{\sum_j F_{+,j}^2 + F_{\times,j}^2}$ (Finn 2001; Schutz 2011), as a function of sky position in equatorial coordinates at time t . The red, green, and blue crosses mark the locations of the three injected M_* galaxies at 1000 Mpc, 750 Mpc, and 500 Mpc (Table 2), respectively, used in Grid I. The lime green and white circles denote the “bright” (maximum sensitivity) and “dark” (minimum sensitivity) sky locations in panels (A) and (C) (Table 3), respectively, selected based on the network antenna pattern and used in Grid II.

Table 3. Sky coordinates for Grid II, corresponding to the most and least sensitive points on the antenna response pattern for each detector network (HLVKIEC, HLV, and EC). The sensitivity is quantified by the combined antenna power $\sum_j \sqrt{(F_{+,j}^2 + F_{\times,j}^2)}$, computed over the full sky at a fixed geocentric time $t_c = 0.0$ and polarization angle $\psi = 0$. The *maximum* sensitivity represent directions of peak network response to GWs, while the *minimum* sensitivity correspond to minima in directional sensitivity.

Network	Sensitivity	RA (deg)	Dec (deg)
HLVKIEC	Maximum	279.000	-48.923
	Minimum	68.203	-12.025
EC	Maximum	286.967	-44.202
	Minimum	238.359	19.471

Table 4. Fixed injection parameters in the BILBY runs. For each run, $m_1 = m_2 = [50.0, 40.0, 30.0, 20.0, 10.0, 5.0] M_\odot$, and the sky position coordinates (RA, Dec) vary according to Tables 2, 3.

Parameter	Injected Value	Units
Spin magnitude 1, a_1	0.1	–
Spin magnitude 2, a_2	0.1	–
Tilt angle 1, θ_1	0.0	rad
Tilt angle 2, θ_2	0.0	rad
Azimuthal spin angle, ϕ_{12}	0.0	rad
Precession angle, ϕ_{JL}	0.0	rad
Inclination angle, θ_{JN}	0.4	rad
Polarization angle, ψ	0.0	rad
Coalescence phase, ϕ_c	0.0	rad
Geocentric time, t_c	0.0	s

Table 5. Priors and their ranges used in the BILBY runs. Parameters not listed here are fixed to their injected values (Table 4).

Parameter	Prior Range	Units
Right Ascension, RA	$[0, 2\pi]$	rad
Declination, Dec	$[-\pi/2, \pi/2]$	rad
Geocentric time, t_c	$[-0.5, 0.5]$	s
Luminosity distance, d_L	$[1, 10000]$	Mpc
Inclination angle, θ_{JN}	$[0, \pi]$	rad
Polarization angle, ψ	$[0, \pi]$	rad
Coalescence phase, ϕ_c	$[0, 2\pi]$	rad

merger environment are not necessarily identical (e.g. Mapelli 2020). As a first-order approximation, we can assume that the likelihood of a galaxy hosting a BBH merger is proportional to its stellar mass. In the local Universe ($\lesssim 1000$ Mpc), most of the stellar mass is concentrated around M_* , the characteristic break in the galaxy stellar mass function (see below). However, given the strong relationship between the galaxy stellar mass and metallicity (Tremonti et al. 2004), systems formed preferentially at low metallicity should also form in low mass galaxies. Alternatively, since the bulge mass and the number of GCs per unit stellar mass increases for more massive galaxies, those formed via dynamical interactions may be formed preferentially in more massive galaxies. We do not attempt to model this fully here, but consider characteristic (if simplistic) models that may capture the range of plausible behaviour.

To implement this approach, we begin with the galaxy stellar mass function (GSMF) as described by the double Schechter function (Schechter 1976):

$$\Phi(M)dM = \left[\phi_1 \left(\frac{M}{M_*} \right)^{\alpha_1} + \phi_2 \left(\frac{M}{M_*} \right)^{\alpha_2} \right] e^{-M/M_*} \frac{dM}{M_*}, \quad (1)$$

where M is the stellar mass of the galaxy, $\Phi(M)dM$ is the number

Table 6. GSMF parameters for galaxies in various surveys over different redshifts.

Ref.	z	$\log(M_*/M_\odot)$	ϕ_1	ϕ_2	α_1	α_2
B12	< 0.06	10.66	3.96	0.79	-0.35	-1.47
W16	0.02 - 0.06	10.79	0.49	0.98	-1.69	-0.79
M21	0.25 - 0.75	10.64	2.34	0.78	0.25	-1.49
	0.75 - 1.25	10.51	2.14	0.85	0.08	-1.49
	1.25 - 1.75	10.54	1.48	0.48	-0.07	-1.60
	1.75 - 2.25	10.56	0.89	0.31	-0.06	-1.63
	2.25 - 2.75	10.55	0.53	0.32	0.02	-1.66
	2.75 - 3.75	10.64	0.08	0.18	0.35	-1.76

Ref.: B12 - [Baldry et al. \(2012\)](#), W16 - [Weigel et al. \(2016\)](#), M21 - [McLeod et al. \(2021\)](#)

Surveys: GAMA (B12), SDSS DR7 (W16), and HST combined with ground-based surveys ([McLeod et al. 2021](#))

density of galaxies per unit stellar mass in the range $(M, M + dM)$, M_* is the characteristic stellar mass which represents the transition between the power-law and exponential regimes, ϕ_1 and ϕ_2 are the normalization constants for the high-mass and low-mass ends respectively, and α_1 and α_2 are the power law slopes of the high-mass and low-mass ends, respectively. To compute the number density of galaxies in a specific mass range (M_1, M_2) , we integrate Equation 1 over those limits. Observational values for the Schechter parameters $(M_*, \phi_1, \phi_2, \alpha_1, \alpha_2)$ are drawn from various galaxy surveys, including GAMA ([Baldry et al. 2012](#)), SDSS DR7 ([Weigel et al. 2016](#)), and high-redshift samples from the Hubble Space Telescope (HST) and other ground-based observatories ([McLeod et al. 2021](#)) (see Table 6).

While the GSMF captures the overall stellar mass distribution of galaxies, different BBH formation channels weigh this distribution differently based on their host environment preferences. We first consider the isolated formation channel. [Santoliquido et al. \(2022\)](#) provide empirical fits for the BBH merger rate per galaxy per year, n_{iso} ³, across a range of stellar masses and redshifts⁴. These fits, based on population synthesis models, incorporate either the galaxy mass-metallicity relation (MZR) or the fundamental metallicity relation (FMR). As both yield similar BBH merger rate densities for $z < 1$, we adopt the MZR-based values for our analysis (see their table 2 and figure 13).

We then normalize the BBH merger rate such that $n_{\text{iso}} \in [0, 1]$ and define an efficiency-weighted GSMF:

$$\Phi^{\text{iso}}(M, z) = n_{\text{iso}}(M) \Phi(M, z). \quad (2)$$

To model the dynamical channel, we assume that BBHs originate from interactions in GCs. In this case, the BBH formation efficiency would follow an empirical power-law relation between the galaxy stellar mass and the number of GCs. To account for this, we adopt a stellar mass–GC scaling relation to weigh the GSMF, thereby constructing a dynamical efficiency-weighted GSMF. The number of GCs per galaxy with $M > 10^{10} M_\odot$ is well described by a power-law scaling relation ([Harris et al. 2013, 2014; Zaritsky et al. 2015](#)):

$$n_{\text{GC}}(M) = N_0 \left(\frac{M}{M_0} \right)^\delta, \quad (3)$$

³ $\log(n_{\text{iso}}/\text{Myr}^{-1}) = a + b \log(M/M_\odot)$

⁴ We assume the model corresponding to common-envelope parameter $\alpha=5$ (see also [Zevin et al. 2021](#) and [Colloms et al. 2025](#)); α quantifies the efficiency with which orbital energy is used to expel the envelope of a star when the two stars in a binary interact closely.

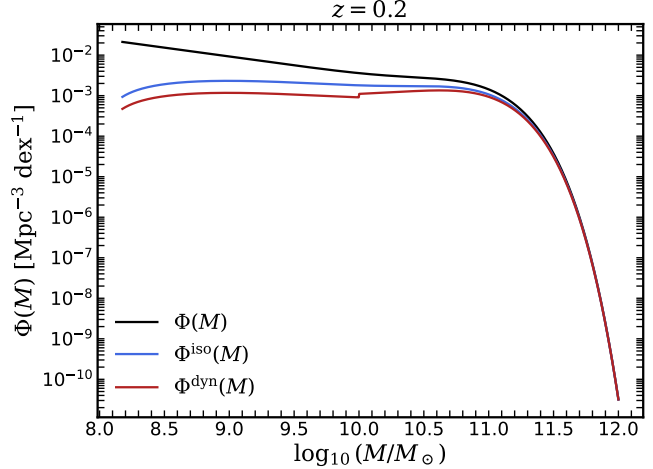


Figure 3. Weighted and unweighted GSMFs at $z = 0.2$; The black curve shows the original GSMF $\Phi(M)$ (Equation 1), modeled using a redshift-interpolated double Schechter function. The blue curve, $\Phi^{\text{iso}}(M)$ (Equation 2), represents the mass function weighted by a BBH merger efficiency model for the isolated formation channel, normalized over stellar mass. The red curve, $\Phi^{\text{dyn}}(M)$ (Equation 4), is weighted by a globular cluster (GC) scaling relation to represent dynamical BBH formation.

where M is the stellar mass of a galaxy, M_0 is a reference mass, N_0 is a normalization constant, and δ is the power-law slope. For $M > 10^{10} M_\odot$, we adopt $\log N_0 = 2.924$, $\log(M_0/M_\odot) = 11.2$, and $\delta \approx 1$ ([Harris et al. 2013](#)). For lower-mass galaxies ($10^8 \leq M/M_\odot \leq 10^{10}$), the relation flattens, with $\delta = 0.365$, $\log N_0 = 1.274$, and $\log(M_0/M_\odot) = 9.2$. As before, we normalize $n_{\text{GC}}(M)$ such that $n_{\text{GC}}(M) \in [0, 1]$ and define the dynamical efficiency-weighted GSMF:

$$\Phi^{\text{dyn}}(M, z) = n_{\text{GC}}(M) \Phi(M, z). \quad (4)$$

Figure 3 illustrates the original GSMF $\Phi(M)$, and the weighted GSMFs: $\Phi^{\text{iso}}(M)$ and $\Phi^{\text{dyn}}(M)$ at $z = 0.2$. The isolated BBH formation channel yields a broad and uniform distribution across galaxy stellar masses, whereas the dynamical channel shows a relative preference for higher-mass galaxies, reflecting the scaling of the number of GCs with galaxy mass.

2.6 Theoretical Localization Volumes

To evaluate the prospects for uniquely identifying the host of a BBH merger, we compare the simulated GW localization volume to the expected number density of galaxies within that same volume. In particular, we evaluate the minimum comoving volume that must be achieved in order to uniquely associate a galaxy of stellar mass M_* with the BBH merger. This provides a theoretical upper bound on the localization volume necessary for host identification, under the assumption of a specific BBH formation channel.

We assume that galaxies are distributed homogeneously and isotropically in space, following the cosmological principle. While true on large scales and a standard approximation (e.g. [Dodelson et al. 1997](#)), we note that on small scales, this approximation necessarily breaks down. True localization volumes are likely not within this limit (at least not when they are sufficiently small to yield host identifications); hence, this approach is necessarily an approximation. Given a GSMF, $\Phi(M, z)$ (Equation 1), we compute the expected number of galaxies with stellar masses $\geq M$ contained within a comoving

Table 7. Minimum volume required to observe, on average, at least 1 galaxy of mass M (equal to the injected host masses at each corresponding redshift, see Table 2) (V_{\min}) for each BBH formation channel. Units are in Mpc^3 .

Channel	500 Mpc	750 Mpc	1000 Mpc
V_{\min}	2.7×10^3	2.1×10^3	1.2×10^3
V_{\min}^{iso}	3.6×10^3	2.7×10^3	1.5×10^3
V_{\min}^{dyn}	4.1×10^3	3.2×10^3	1.8×10^3

volume V by assuming Poisson statistics. The minimum comoving volume required to contain, on average, λ such galaxies is then

$$V_{\min}(\geq M, z) = \frac{\lambda}{\int_{\log_{10} M}^{\infty} \Phi(M', z) d \log_{10} M'}, \quad (5)$$

where the denominator represents the cumulative comoving number density of all galaxies with stellar masses $\geq M$. This cumulative form reflects the fact that we do not know *a priori* which galaxy within a localization volume is the true host.

A localization volume equal to $V_{\min}(\lambda = 1)$ corresponds to an expectation value of, on average, one galaxy of mass M_* ; volumes smaller than this may still contain such a galaxy, but the average number falls below unity (Figure 4).

To account for different astrophysical channels of BBH formation, we compute analogous minimum comoving volumes using the modified GSMEs introduced earlier in Section 2.5. For the isolated and dynamical channels, Equation 5 is evaluated using $\Phi^{\text{iso}}(M, z)$ (Equation 2) and $\Phi^{\text{dyn}}(M, z)$ (Equation 4), resulting in corresponding minimum localization volumes, $V_{\min}^{\text{iso}}(M, z)$ and $V_{\min}^{\text{dyn}}(M, z)$, respectively. Each of these volumes - V_{\min} , V_{\min}^{iso} , and V_{\min}^{dyn} - can be interpreted as the minimum localization volume required to statistically isolate, on average, a single galaxy of stellar mass M_* ($\lambda = 1$) under the assumption of the corresponding BBH formation channel. We note, importantly, that $\lambda = 1$ is the point at which we expect one galaxy within the localization volume at random. Hence, it is not a volume at which we can realistically claim (at least not with high confidence) to be able to identify the host. We consider this further in Section 3.

2.6.1 Metallicity Dependence

Several binary population synthesis models predict that BBH formation via isolated binary evolution is strongly dependent on progenitor metallicity (e.g. Belczynski et al. 2010; Eldridge & Stanway 2016), with lower-metallicity environments favouring the formation of more massive BHs and higher merger rates (e.g. Giacobbo et al. 2018; Spera et al. 2019). In contrast, dynamical formation channels are largely insensitive to metallicity (e.g. Mapelli et al. 2022). This distinction presents a potential way to distinguish BBH formation channels. Analysis by Zevin et al. (2021) (see also Bouffanais et al. 2021) indicates that no single formation pathway accounts for more than $\sim 70\%$ of the BBHs detected in GWTC-2.0 and GWTC-2.1 (Abbott et al. 2021a, 2024). Recent population synthesis studies suggest that the isolated channel may contribute a larger fraction than the dynamical channel (Barber & Antonini 2025).

To explore how metallicity may influence our analysis, we adopt a representative metallicity threshold of $12 + \log(\text{O/H}) = 8.3$, commonly found as a threshold for the occurrence of long gamma-ray bursts (LGRBs) (e.g. Graham & Fruchter 2017). The relation between galaxy stellar mass and metallicity is captured by the MZR relation of Zahid et al. (2014), valid for $z \lesssim 1.6$ and parameterized

as:

$$12 + \log(\text{O/H}) = Z_0 + \log \left[1 - \exp \left(- \left[\frac{M_*}{M_0} \right]^\gamma \right) \right], \quad (6)$$

where Z_0 is the saturation metallicity (e.g. Moustakas et al. 2011); M_0 is the characteristic turnover galaxy mass above which the metallicity asymptotically approaches the upper metallicity limit $Z_0 = 9.102$ and $\gamma = 0.513$ is the power-law index (values taken from table 2 in Zahid et al. 2014). The MZR flattens at high galaxy stellar masses at $z = 0.2$. Using this relation, we find that this threshold corresponds to a galaxy stellar mass of $\log(M/\text{M}_\odot) = M_Z = 7.97$. We then treat this mass as a lower threshold and compute the number density of galaxies with stellar mass $\geq M_Z$, using a method analogous to that described in Section 2.6. This yields $\Phi^Z = 1.84 \times 10^{-2} \text{ Mpc}^{-3}$, and an associated minimum localization volume of $V_{\min}^Z = 54.42 \text{ Mpc}^3$.

3 PRESCRIPTIONS FOR HOST GALAXY IDENTIFICATION FOR BBH MERGERS

3.1 Masses within the GW Localization Volumes

We compare the injected host to the total stellar mass in galaxies within the GW localization volume. We compute the total stellar mass enclosed in two ways: a theoretical estimate based on the GSME, and an observational estimate obtained by summing the stellar masses of galaxies in galaxy catalogues within the localization region, although we note that, at least at the current time, the latter approach is of very limited value because of galaxy catalogue incompleteness.

3.1.1 Theoretical Galaxy Stellar Mass

To estimate the total stellar mass theoretically enclosed within a GW localization region, we proceed as follows. We compute the stellar mass density, $\rho_\star(z) [\text{M}_\odot \text{ Mpc}^{-3}]$ by computing the mass-weighted integral of the GSME, $\Phi(M)$, over a stellar mass range of $(M_{\min}, M_{\max} = 10^8 \text{ M}_\odot, 10^{12} \text{ M}_\odot)$:

$$\rho_\star(z) = \int_{M_{\min}}^{M_{\max}} M \Phi(M) dM. \quad (7)$$

The total expected stellar mass enclosed within the GW localization region is $M_\Phi(z) = \rho_\star V_{\text{comoving}}$. This formalism enables the computation of the theoretical stellar mass contained within the V_{50} and V_{90} credible regions of each injection.

3.1.2 Observed Galaxy Stellar Mass

We determine the total observed mass enclosed within the GW localization volume by first performing a 3D crossmatch of the GW localization volumes with the NED-LVS galaxy catalogue, and then defining:

$$M_{\text{obs}} = \sum_{i=1}^N M_{\text{candidate},i}, \quad (8)$$

where $M_{\text{candidate},i}$ denotes the stellar mass of the i^{th} galaxy identified within the localization volume, and N is the total number of crossmatched candidates from the NED-LVS galaxy catalogue.

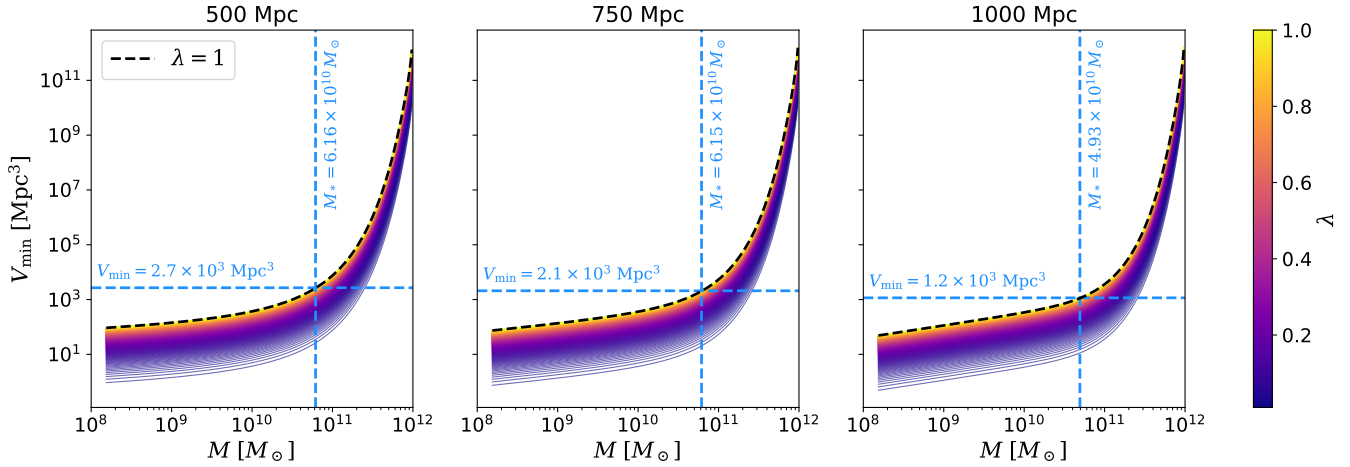


Figure 4. Minimum comoving volumes V_{\min} required to contain, on average, one galaxy of mass M as a function of galaxy stellar mass and redshift. Each panel corresponds to a different injected host at distances of 500 Mpc, 750 Mpc, and 1000 Mpc. Coloured curves show $V_{\min}(M)$ (Equation 5) scaled by different values of λ . The black dashed line denotes the fiducial case of $\lambda = 1$. The vertical blue dashed line marks the mass of the injected M_* galaxy (Grid I, Table 2), while the horizontal blue dashed line indicates the corresponding V_{\min} value at that mass. All three curves assume the redshift-dependent GSMF $\Phi(M, z)$ (Equation 1).

3.1.3 Mass Fractions

To quantify the significance of the injected M_* host relative to the total galaxy stellar mass within the GW localization volume, we define two complementary dimensionless mass fractions:

- (i) $\mathbb{M}_{*,\Phi}$: We compare the stellar mass of the injected M_* host to the total theoretical mass enclosed within the GW localization volume by computing the theoretical mass fraction, $\mathbb{M}_{*,\Phi} = M_*/M_\Phi$.
- (ii) $\mathbb{M}_{*,\text{obs}}$: Similarly, we compute an observed mass fraction, $\mathbb{M}_{*,\text{obs}} = M_*/M_{\text{obs}}$, where M_{obs} is the total stellar mass of all candidate hosts identified within the GW localization volume.

3.2 Probability of Chance Alignment

A common way to assess the significance of a candidate host association is the probability of chance alignment, p_c . This quantifies the likelihood that a galaxy of a certain brightness falls at a certain proximity to the source location at random. It is calculated through a combination of the offset and magnitude of the putative host based on the 2D distribution of galaxies on the sky. In particular, Bloom et al. (2002) define $P_c = 1 - \exp(-\eta_i)$. Here η_i is the expected number of galaxies as bright as or brighter than the candidate host within a certain search region. In the traditional 2D case, this is given by $\eta_i = \pi r^2 \sigma_i$, where r is the angular separation from the transient and σ_i is the surface density of galaxies as bright as or brighter than the host.

In the context of GW follow-up, the projected 2D density of galaxies across the sky becomes extremely high due to the large localization areas. However, as the measurement of the luminosity distance is also available, this information should be used as well. The total number of galaxies within the 3D localization volume (i.e., within the luminosity distance and sky position uncertainty) may be tractable.

We therefore define η_i to account for the number of galaxies with stellar mass equal to or greater than that of the candidate host, M_{host} , within a comoving volume V :

$$\eta_i(\geq M_{\text{host}}) = V \int_{M_{\text{host}}}^{\infty} \Phi(M) dM \quad (9)$$

where $\Phi(M)$ is the GSMF (Equation 1). Here, we consider both the V_{50} and V_{90} credible volumes for V , and also the weighted GSMFs corresponding to the different BBH formation channels, Φ_{\min}^{iso} (Equation 2) and Φ_{\min}^{dyn} (Equation 4).

Alternatively, a luminosity-based formulation can be used:

$$\eta_i(\geq L_{\text{host}}) = V \int_{L_{\text{host}}}^{\infty} \Phi(L) dL, \quad (10)$$

where $\Phi(L)$ is the galaxy luminosity function and L_{host} is the luminosity of the candidate host.

4 RESULTS

4.1 Grid I: Galaxy Catalogue Injections

4.1.1 Localization Volumes

Figure 5 presents the 3D localization volumes, quantified by the V_{50} and V_{90} credible regions, for each BBH injection in Grid I (Table 2), as inferred for the three GW detector networks we consider: HLVKIEC, HLV, and EC. Consistent with expectations, the HLVKIEC and EC networks yield significantly smaller localization volumes than HLV, due to their enhanced detector sensitivity and correspondingly higher SNR values for the CBCs. At fixed network and distance, localization volumes increase with decreasing total mass of the binary due to the correlation between SNR and CBC masses (Figure 1). For high-mass binaries, such as 50+50 M_\odot , $V_{90}^{\text{HLVKIEC}} \sim V_{90}^{\text{EC}} \sim 10^{-1} \text{ Mpc}^3$ at 500 Mpc, and $V_{90}^{\text{HLVKIEC}} \sim V_{90}^{\text{EC}} \sim 10 \text{ Mpc}^3$ at 1000 Mpc. In contrast, the HLV network yields much poorer localization, with $V_{90}^{\text{HLV}} > 10^2 \text{ Mpc}^3$ across all the distances and mass configurations.

The horizontal shaded bands in Figure 5 indicate the theoretical minimum comoving volumes required to contain, on average, one galaxy of mass M_* or higher, under the assumption of different BBH formation channels as defined in Section 2.6, along with the metallicity-based threshold V_{\min}^Z that we defined in Section 2.6.1. Across both 50% and 90% credible volumes, the EC and HLVKIEC networks demonstrate strong localization performance relative to the

threshold volumes, with localization volumes consistently lower than the thresholds across all mass configurations and distances; only at the lowest mass configuration at 1000 Mpc, V_{90}^{HLVKIEC} and V_{90}^{EC} are above V_{\min}^Z .

4.1.2 Mass Fractions

Figure 6 shows the theoretical mass fractions, $\mathbb{M}_{*,\Phi}$, for each BBH injection in Grid I. Both HLVKIEC and EC networks yield values of $\sim 1 - 10^4$ at all three distances, for values evaluated with both V_{90} and V_{50} , with a systematic decline towards 1000 Mpc and towards low-mass BBHs; for HLV, $\mathbb{M}_{*,\Phi}$ is a few orders of magnitudes smaller ($\sim 10^{-3} - 10$), reflecting the larger localization volumes in those cases. The corresponding observed mass fractions, $\mathbb{M}_{*,\text{obs}}$, are discussed in Section 5.2.3.

4.1.3 Chance Alignment

We evaluate the probability of chance alignment, p_c (Section 3.2), as a diagnostic of host identification for the BBH injections in Grid I in Figure 7. At 500 Mpc, both EC and HLVKIEC consistently yield low chance alignment values, with $p_c < 0.01$ for all mass configurations and GSMEs. In contrast, HLV shows higher values, with $p_c(V_{90}) > 0.8$ for the 5+5 M_\odot injection. At 750 Mpc, the difference between the detector networks becomes more distinct. Both EC and HLVKIEC maintain $p_c < 0.01$ for all mass configurations. The HLV-only configuration performs comparatively poorly, with $p_c(V_{90}) > 0.2$ for the 50+50 M_\odot injection and $p_c(V_{90}) \sim 1$ at 5+5 M_\odot . At 1000 Mpc, $p_c(V_{90}) \lesssim 0.01$ for all the HLVKIEC and EC injections up to 10+10 M_\odot , and increases to ~ 0.1 at 5+5 M_\odot . HLV returns $p_c \approx 1$ across all injections at 1000 Mpc.

4.2 Grid II: Maximum & Minimum Sky Sensitivity Injections

4.2.1 Localization Volumes

Figure 8 illustrates the impact of network directional sensitivity on localization performance by comparing the credible volumes, V_{50} and V_{90} , for HLVKIEC and EC, at sky locations corresponding to maximum and minimum antenna responses (Table 3). As discussed in Section 2.2, these sky positions were determined from the "bright" and "dark" regions of the antenna patterns of each detector network, and they approximately represent the most and least favourable configurations for network sensitivity, enabling us to probe the full range of localization outcomes for a fixed set of intrinsic source parameters.

Panels (a-c) in Figure 8 show the localization volumes for the injected sources at the *maximum sensitivity* points of each network (lime green circles in Figure 2, also see Table 3). In this best-case scenario, both networks localize all the injections across all the distances to volumes similar to or less than the threshold comoving volumes (V_{\min} , V_{\min}^{iso} , V_{\min}^{dyn}). For instance, a 50+50 M_\odot BBH merger at 500 Mpc has $V_{50}^{\text{HLVKIEC}} \sim V_{50}^{\text{EC}} \sim 10^{-1} \text{ Mpc}^3$. Across the distances, HLVKIEC shows slightly better localization performance than EC. At 500 Mpc, both networks have localization volumes $< V_{\min}^Z$; at higher distances, the lowest mass configurations are localized to volumes $\gtrsim V_{\min}^Z$.

Panels (d-f) present results from the *minimum sensitivity* sky locations (white circles in Figure 2; also see Table 3). Localization performance slightly deteriorates in these regions, particularly for the low-mass systems and at 1000 Mpc. All the injections, except 5+5 M_\odot at 1000 Mpc, have localization volumes less than the threshold comoving volumes. Notably, EC performs uniformly better than

HLVKIEC in this case, we discuss this effect in detail in Section 5.1. At 500 Mpc, the localization volumes are $< V_{\min}^Z$ but at higher distances, heavier BBH systems have the localization volumes $\gtrsim V_{\min}^Z$, especially for V_{90}^{HLVKIEC} .

4.2.2 Mass Fractions

Figure 9 shows the theoretical mass fractions, $\mathbb{M}_{\text{host},\Phi}$, calculated for the Grid II injections. For the *maximum sensitivity* injections (Panels a-c), $\mathbb{M}_{\text{host},\Phi}$ is $\sim 10^2 - 10^3$ for most injections at 500 Mpc, falling to $\sim 10 - 10^2$ at 1000 Mpc; lighter BBH mergers have values ~ 1 . For the *minimum sensitivity* injections (Panels d-f), the fractions are lower by an order of magnitude across the grid, with most injections at 1000 Mpc, evaluated with V_{90} , having values ≈ 1 . Large values such as $\mathbb{M}_{\text{host},\Phi} \sim 100$ imply that the volume contains less than one M_* galaxy, i.e., $M_\Phi \approx 0.01 M_{\text{host}}$. Observed mass fractions, $\mathbb{M}_{\text{host,obs}}$, are not calculated for Grid II because the sky positions of the injected galaxy do not correspond to the NED-LVS galaxy catalogue.

4.2.3 Chance Alignment

We evaluate the probability of chance alignment, p_c (Section 3.2), for the Grid II injections, shown in Figure 10. At the *maximum sensitivity* locations (Panels a-c), both HLVKIEC and EC yield uniformly small values across all distances ($p_c < 0.01$); at 1000 Mpc, there is a slight increase for 10+10 ($p_c \approx 0.1$) and 5+5 M_\odot ($p_c \gtrsim 0.2$) injections.

At the *minimum sensitivity* locations (Panels d-f), both networks yield small values up to 750 Mpc, with a slight increase ($p_c \sim 0.1$) for the 5+5 M_\odot injection at 750 Mpc. At 1000 Mpc, the values increase slightly ($p_c \sim 0.1$) for the heavier BBH systems and significantly for the lighter systems ($p_c \lesssim 0.2$ for 10+10 M_\odot ; $p_c \sim 0.2 - 0.6$ for 5+5 M_\odot).

Across panels, HLVKIEC and EC track each other closely; p_c values vary very slightly with mass, sky location, and BBH formation channels. Overall, chance alignments are rare for nearby, high-mass events at favourable sky positions, but become probable for lighter binaries at larger distances and at minimum-sensitivity locations.

5 DISCUSSION

5.1 GW Detector Network Comparison

A key objective of this work is to assess the extent to which 3G GW detector networks can localize stellar-mass BBH mergers to volumes small enough to enable unique M_* host identification (referred to as "host" hereafter) and, subsequently, constrain BBH formation channels and cosmological measurements such as H_0 . Our simulated BBH merger injections extend out to 1000 Mpc ($z \sim 0.23$), sampling a region that typically overlaps with the higher SNR of the observed GW parameter space (Figure 11). Across both injection grids I and II (Section 2.2) and across all distances up to 1000 Mpc, we find that incorporating 3G detectors, ET and CE, dramatically improves localization performance relative to current-generation detector networks, with localization volumes typically less than the defined theoretical comoving volume thresholds. It should be noted, however, that the comoving volume thresholds are defined as an expectation value under the assumption of Poisson statistics for the galaxy distribution; while sub-threshold localization volumes increase the probability of a unique host, they do not guarantee it. Further, we assume ET has a configuration of an equilateral triangle with 10 km arms in our

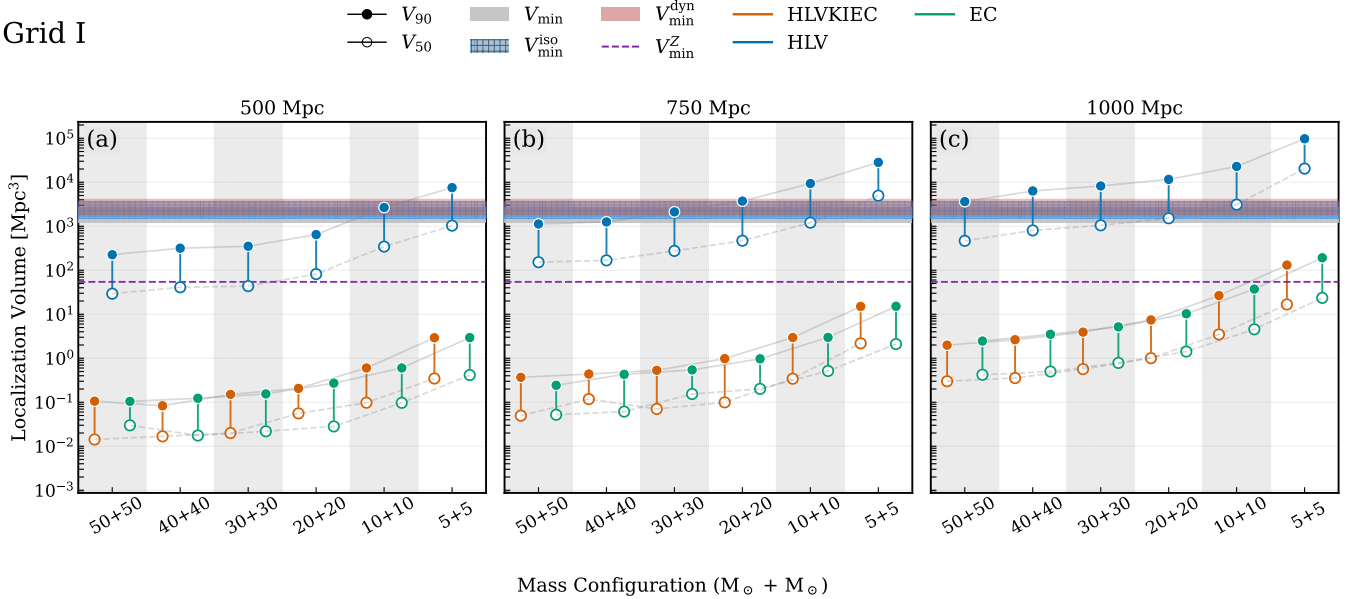


Figure 5. Localization volumes for simulated BBH mergers in Grid I, at luminosity distances of 500, 750, and 1000 Mpc (Panels *a–c*). For each mass configuration and network: HLVKIEC (red), HLV (blue), EC (green), we plot V_{50} (hollow marker) and V_{90} (filled marker), with a vertical line connecting the two. Horizontal shaded bands indicate the minimum comoving volume required to contain, on average, one galaxy of mass M_* or higher under three different BBH formation channel assumptions: V_{\min} (gray, Equation 5), V_{\min}^{iso} (blue), and V_{\min}^{dyn} (red). These threshold comoving volumes were computed within a redshift range of $z = 0.12$ and $z = 0.23$, corresponding to the injected M_* hosts (Table 7). The dashed purple horizontal line corresponds to the metallicity-dependent minimum comoving volume, $V_{\min}^Z = 370.70 \text{ Mpc}^3$, as calculated in Section 2.6.1.

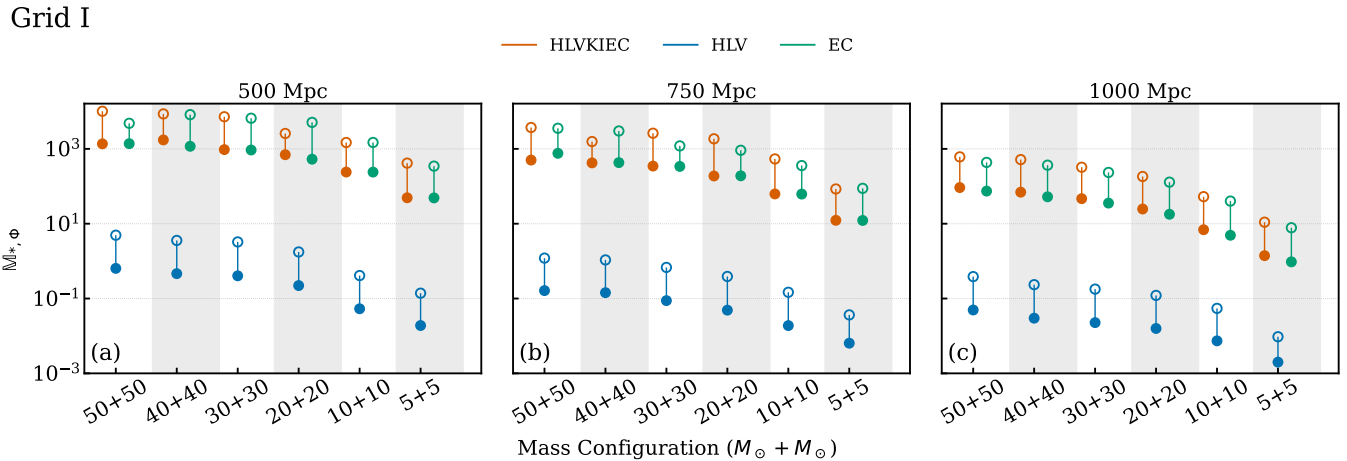


Figure 6. Theoretical ($M_{\text{host},\Phi}$) mass fractions (Section 3.1) for simulated BBH mergers in Grid I at 500 Mpc, 750 Mpc and 1000 Mpc (Panels *a–c*). $M_{\text{host},\Phi}$ is the ratio between the mass of the injected M_* galaxy and the total theoretical mass enclosed within the GW localization volumes V_{50} and V_{90} . Colours denote the GW detector networks: HLVKIEC (red), HLV (blue), EC (green). The hollow markers correspond to values evaluated within the V_{50} region and the filled markers correspond to values evaluated within the V_{90} region.

simulations. [Branchesi et al. 2023](#) showed that two L-shaped ET detectors with 15 km arms, separated by ~ 1000 – 2000 km, is likely to provide an improved (i.e. reduced) distance uncertainty over a single triangular ET detector with 10 km arms, while additional baselines provide further improved sky-localisation. The results presented in this paper are therefore, likely conservative in the sense that this reduced uncertainty will likely lead to smaller localization volumes in the two detector configuration. To quantify this effect fully is beyond the scope of this paper.

Grid I examines how localization performance scales with the mass configurations and distances, by fixing the injections to M_* galaxies at 500, 750, and 1000 Mpc (Table 2). Within this framework, both HLVKIEC and EC networks consistently achieve sub-threshold localization volumes (Figure 5). In contrast, the HLV network produces substantially larger localization volumes, with $V_{90}^{\text{HLV}} \sim 10^2$ – 10^5 Mpc^3 , and thus rarely supports confident host associations or formation channel-based constraints. These results must be interpreted in the context of the underlying FIM-based PE method

Grid I

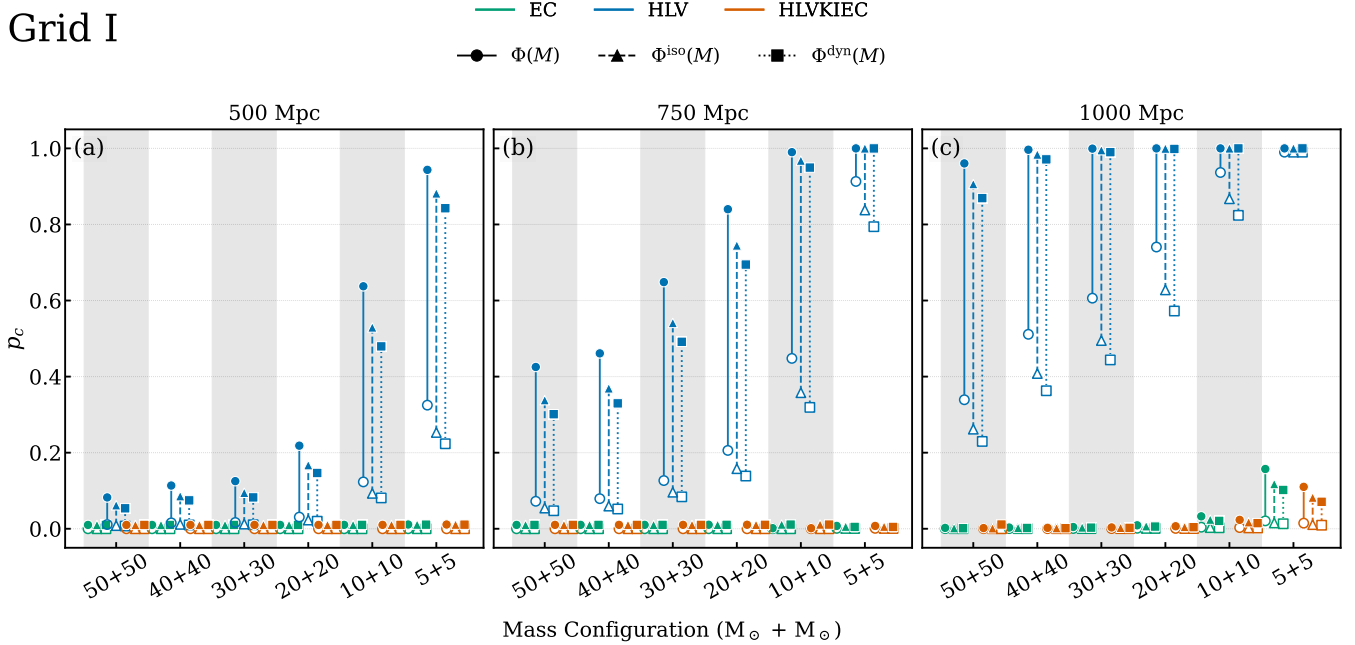


Figure 7. Probability of chance alignment, p_c , for Grid I BBH injections at 500 Mpc, 750 Mpc, and 1000 Mpc (Panels a-c). Colours denote the GW detector networks: HLVKIEC (red), HLV (blue), EC (green). The line style/marker encodes the different GSMFs across BBH formation channels used in Equation 9: $\Phi(M)$ (solid/circle, Equation 1), $\Phi^{\text{iso}}(M)$ (dashed/triangle, Equation 2), $\Phi^{\text{dyn}}(M)$ (dotted/square, Equation 4). For each injection, the vertical segment spans the value at V_{50} (hollow marker) to the value at V_{90} (filled marker).

that is valid in the high-SNR limit, where posterior distributions are sharply peaked and approximately Gaussian. These conditions are met by all injections in the HLVKIEC and EC networks, but not for all the HLV injections.

In addition to Grid I, Grid II explores the role of detector geometry by sampling sky locations within the most and least sensitive regions of the EC and HLVKIEC antenna patterns (Figure 2). This enables a direct assessment of how localization volumes vary with directional sensitivity (Figure 8). Both HLVKIEC and EC networks exhibit degraded localization in the "dark" regions of their antenna patterns. Importantly, the comparison between the networks depends on how these minimum- and maximum-sensitivity sky positions are defined. These locations are computed independently for each network and as a result, the minimum-sensitivity sky position of HLVKIEC does not necessarily correspond with the combined minimum of ET and CE individually. In such cases, HLVKIEC may appear to perform worse than EC (Panels d - f in Figure 8), but this is a consequence of the choice of these sky positions.

Together, the Grid I and Grid II results show that future GW detector networks will enable targeted galaxy follow-up campaigns for a significant fraction of BBH mergers. In the best cases, especially for massive BBH mergers, the localization volumes are small enough to isolate a unique host. This, in turn, opens a pathway for associating BBH mergers with specific galaxy populations and statistically distinguishing between formation scenarios, such as isolated evolution and dynamical assembly.

5.2 Implications for Host Identification and Constraining BBH Formation Channels

5.2.1 BBH Formation Channel Constraints from Theoretical Comoving Volume Thresholds

In addition to assessing the feasibility of host identification, comparisons between the simulated localization volumes and the theoretical thresholds V_{\min} (Equation 5), V_{\min}^{iso} , and V_{\min}^{dyn} provide insights into the underlying BBH formation channels (Figures 5 and 8). As defined in Section 2.6, each threshold volume represents the minimum comoving volume required to contain, on average, one M_* galaxy, assuming a specific BBH formation channel. V_{\min} corresponds to the unweighted GSMF and serves as a general baseline, while V_{\min}^{iso} and V_{\min}^{dyn} incorporate mass-weighted GSMFs for the isolated and dynamical channels, respectively.

When the credible localization volumes, V_{50} and V_{90} , for a given BBH injection lie below a threshold, host identification may be achieved on an event-by-event basis (under the single M_* host assumption). In contrast, formation-channel inference requires population-level evidence. For instance, a localization volume that falls below V_{\min}^{dyn} but exceeds V_{\min}^{iso} is, on average, more consistent with the dynamical channel than the isolated one. This does not imply definitive channel classification on an event-by-event basis, but rather indicates which channels are statistically compatible with the inferred host environment, assuming a single M_* host. It is important to note that the dynamical channel considered here refers specifically to GCs. As such, it is plausible that a given galaxy could support BBH formation through both isolated and dynamical pathways.

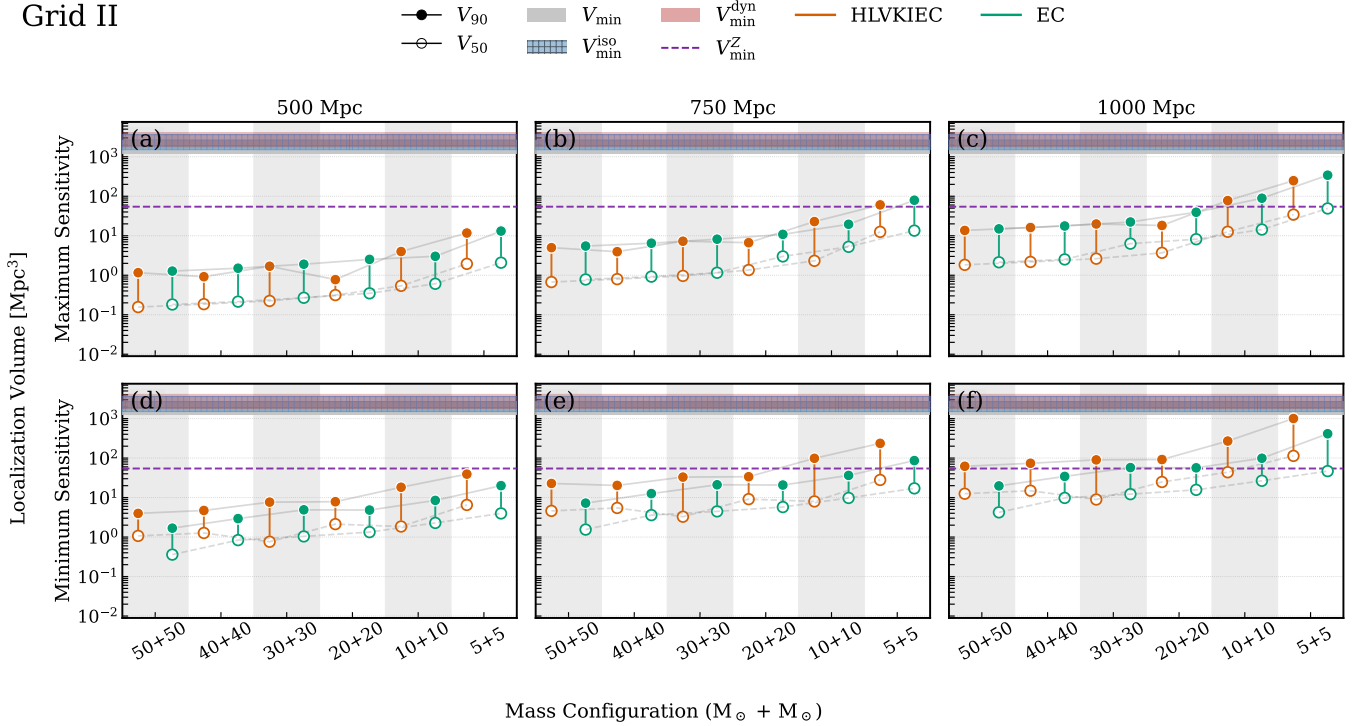


Figure 8. Localization volumes for simulated BBH mergers in Grid II. Top row (Panels a–c) corresponds to the maximum sensitivity injections, and the bottom row (Panels d–f) corresponds to the minimum sensitivity injections (Table 3). Columns correspond to luminosity distances of 500, 750, and 1000 Mpc. For each mass configuration and network: HLVKIEC (red) and EC (green), we plot V_{50} (hollow marker) and V_{90} (filled marker), with a vertical line connecting the two. Horizontal shaded bands indicate the minimum comoving volume required to contain, on average, one galaxy of stellar mass M_* or of a higher mass, under three different BBH formation channel assumptions: V_{\min} (gray, Equation 5), V_{\min}^{iso} (blue), and V_{\min}^{dyn} (red). These reference volumes were computed within a redshift range of $z = 0.12$ and $z = 0.23$, corresponding to the injected M_* hosts (Table 7). The dashed purple horizontal line corresponds to the metallicity-dependent minimum comoving volume, $V_{\min}^Z = 370.73 \text{ Mpc}^3$, as calculated in Section 2.6.1.

5.2.2 Metallicity-Based Constraints

An additional layer of constraint comes from the metallicity dependence of BBH formation. Isolated binary evolution models predict a strong bias toward low-metallicity environments (e.g. Giacobbo et al. 2018; Spera et al. 2019), while dynamical formation channels are comparatively insensitive to progenitor metallicity (e.g. Mapelli et al. 2022). By adopting a representative metallicity threshold of $12 + \log(\text{O/H}) = 8.3$ (Section 2.6.1), we derive a corresponding minimum localization volume, $V_{\min}^Z = 54.42 \text{ Mpc}^3$, below which we expect to detect, on average, one such low-metallicity galaxy. Almost all of the BBH injections localized by the HLVKIEC and EC networks meet this criterion, particularly for high-mass BBH mergers at nearby distances. At higher distances, the low-mass BBH mergers have localization volumes $\gtrsim V_{\min}^Z$ in both Grids I and II. We note that in the low metallicity scenario it may not be possible to identify the host galaxy directly, because there may be fainter, even lower metallicity hosts. However, the absence of bright galaxies in such small localisations would rule out the mergers occurring in such hosts.

5.2.3 Mass Fractions and the Role of Galaxy Catalogue Completeness

We further assess the prominence of the injected host within the GW localization volume using two complementary mass fractions: $\mathbb{M}_{*,\Phi}$ and $\mathbb{M}_{*,\text{obs}}$ (Section 3.1, Figures 6 and 9). The former quantifies the ratio of the mass of the host to the total stellar mass theoretically

expected from the GMSF within the localization volume, while the latter compares the host mass to the total observed stellar mass of galaxies crossmatched with the NED-LVS galaxy catalogue. A value greater than one for either mass fraction increases the plausibility of host identification. In the context of this work, where the injected galaxies are known a priori, it indicates successful recovery of the injected M_* host.

Although $\mathbb{M}_{*,\text{obs}}$ is defined to quantify the observed stellar-mass content within the localization volume, it is governed entirely by the completeness of the underlying galaxy catalogue. For nearly all the injections, we calculate $\mathbb{M}_{*,\text{obs}} \sim 1$, indicating that the crossmatch recovers only the injected host. In contrast, the theoretical mass fraction values, $\mathbb{M}_{*,\Phi}$, are systematically larger, implying that the total stellar mass expected within the localization volume is significantly under-represented in the crossmatched sample. This reflects the incompleteness of the NED-LVS galaxy catalogue at these distances. Further, the incompleteness is also non-uniform: for instance, at 750 Mpc, the 5+5 M_\odot injection yields $\mathbb{M}_{*,\text{obs}} \lesssim 0.1$, whereas at 1000 Mpc, the same mass configuration has a value of $\mathbb{M}_{*,\text{obs}} = 1$. This distance-dependent, non-uniform recovery of galaxies demonstrates that $\mathbb{M}_{*,\text{obs}}$ cannot be meaningfully interpreted without modelling the galaxy catalogue completeness and catalogue selection function.

Grid II

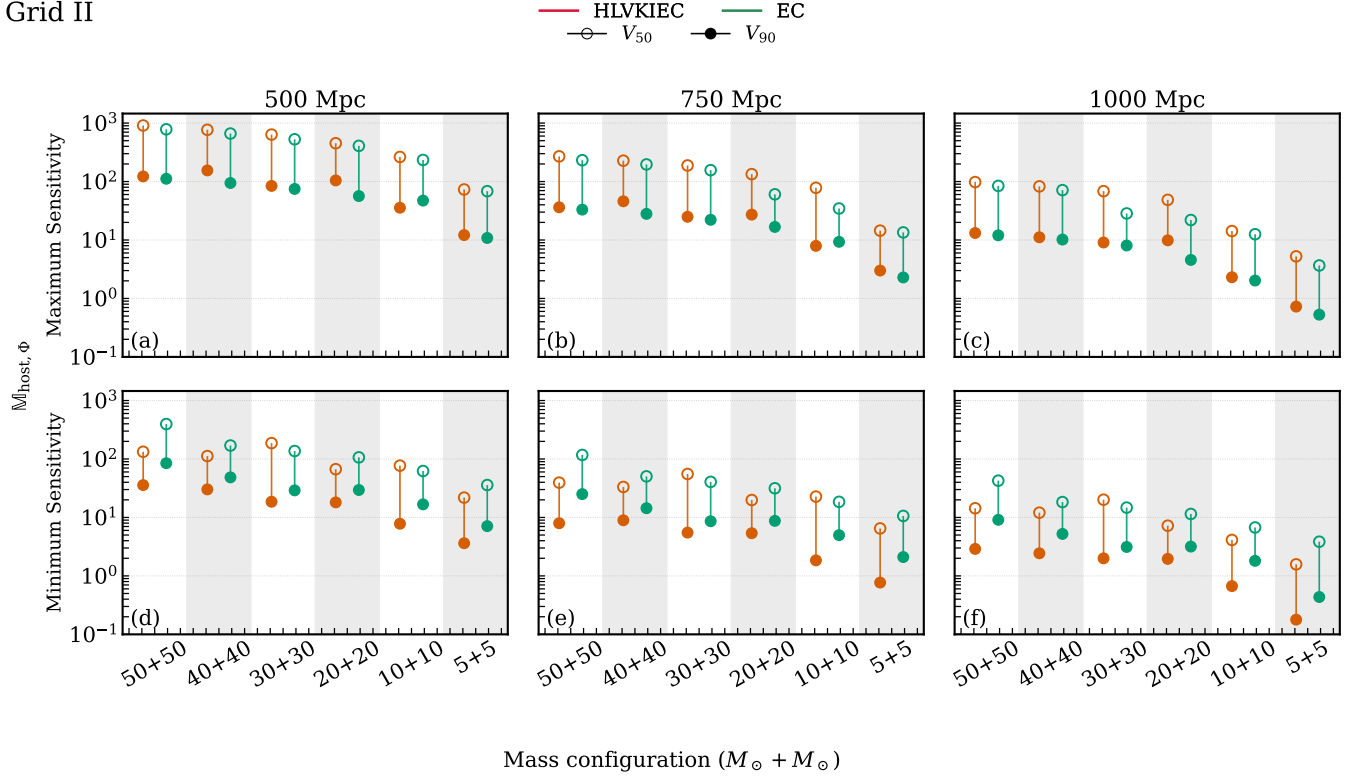


Figure 9. Theoretical mass fractions $M_{\text{host},\phi}$ for Grid II injections. Top row (Panels a - c) corresponds to the maximum sensitivity injections, and the bottom row (Panels d - f) corresponds to the minimum sensitivity injections (Table 3). Columns correspond to luminosity distances of 500, 750, and 1000 Mpc. For each mass configuration and network: HLVKIEC (red) and EC (green), we plot the theoretical mass fraction calculated with V_{90} (filled marker) and V_{50} (hollow marker). Fixed host masses of $M_{\text{host}} = (6.16, 6.15, 4.93) \times 10^{10} M_{\odot}$ are adopted for 500, 750, and 1000 Mpc respectively (as in Grid I).

Grid II

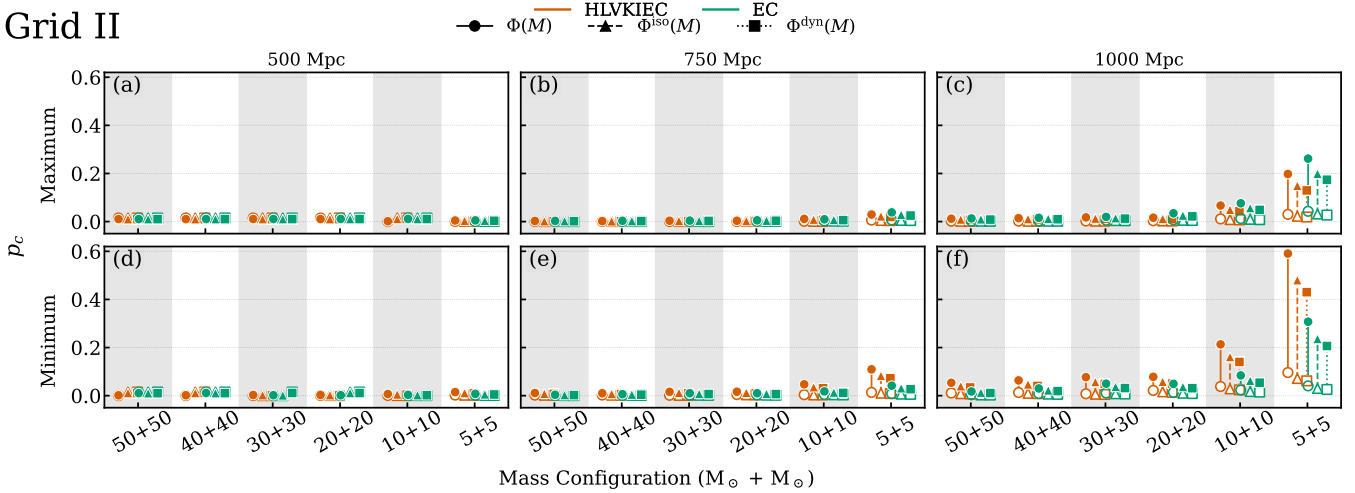


Figure 10. Probability of chance alignment, p_c , for Grid II BBH injections in maximum (top row, Panels a-c) and minimum (bottom row, Panels d-f) sensitivity sky regions, within a range of $p_c = 0 - 0.6$. The three columns (left to right) correspond to 500, 750, and 1000 Mpc. Colours denote the GW detector networks: HLVKIEC (red) and EC (green). The line style/marker encodes the different GSMFs across BBH formation channels used in Equation 9: $\Phi(M)$ (solid, Equation 1), $\Phi^{\text{iso}}(M)$ (dashed, Equation 2), $\Phi^{\text{dyn}}(M)$ (dotted, Equation 4). For each injection, the vertical segment spans the value at V_{50} (hollow marker) to the value at V_{90} (filled marker). The p_c values are computed assuming an injected M_* host at the maximum/minimum sensitivity locations and evaluated against the NED-LVS galaxy catalogue; therefore, very low p_c values (particularly at 500 Mpc) arise because no such galaxy is actually present at those sky positions.

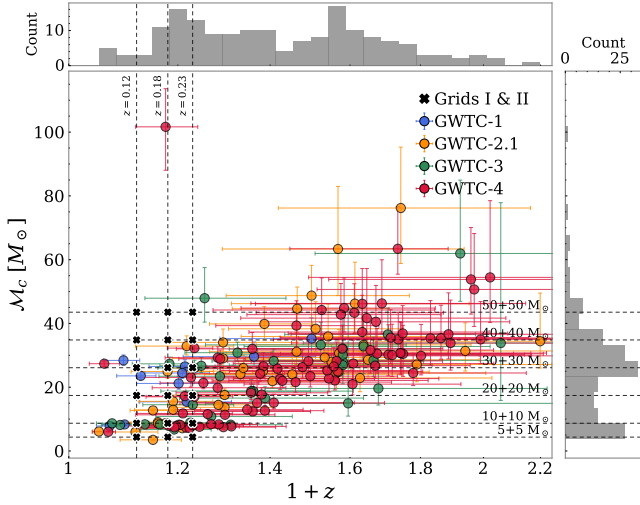


Figure 11. Source-frame chirp mass M_c vs z for BBH events in GWTC-4.0 (Abbott et al. 2019, 2021a, 2024, 2023b; Abac et al. 2025c) (scatter points). Redshifts are computed from the reported luminosity distances using the cosmology adopted in this work. Using the detector-frame chirp mass values $M_{c,\text{det}}$, we recompute the source-frame chirp mass as $M_c = M_{c,\text{det}}/(1+z)$ using those redshifts. The top and right panels give the marginal count histograms in z and M_c . Dashed vertical lines indicate the injection redshifts $z = 0.12, 0.18$, and 0.23 ; dashed horizontal lines indicate the equal-mass injection chirp masses for $m_1 = m_2 = (50.0, 40.0, 30.0, 20.0, 10.0, 5.0) M_\odot$. The black crosses mark the intersections of these grids (Grids I & II, Tables 2 & 3), showing where our injections fall relative to the observed GW population.

5.2.4 Constraints from Chance Alignment Probability

Next, we incorporate the probability of chance alignment, p_c (Section 3.2), to assess whether a galaxy consistent with a given BBH formation channel could arise by random association. As shown in Figures 7 and 10, p_c values computed under $\Phi^{\text{iso}}(M)$ and $\Phi^{\text{dyn}}(M)$ follow a consistent ordering, $p_c^{\text{dyn}} \lesssim p_c^{\text{iso}} \lesssim p_c$, though the differences between channels are typically modest. p_c serves as a valuable consistency check: low values ($\lesssim 0.1 - 0.2$) indicate that a candidate host is unlikely to be a chance superposition, thereby increasing confidence in its association with the BBH merger. Conversely, high p_c values across all GSMFs, as seen for HLV at large distances, indicate that no confident host association and no channel-based inference is possible. While p_c does not independently distinguish formation channels, it improves the reliability of host associations when combined with the theoretical volume thresholds, metallicity cuts, and mass fractions.

5.2.5 Event Rates of BBH Mergers with Identifiable Hosts

Further, we can estimate an event rate per year of BBH mergers with identifiable hosts out to $z \sim 0.23$ in the 3G era. The current generation of GW detectors (HLVK) detects a subset of the entire BBH population with $\text{SNR} \geq 12$ at $z \lesssim 0.1$, with detection efficiency depending on the BH masses and the orientation of the binary with respect to our line-of-sight. In comparison, Iacovelli et al. 2022 estimate that ET alone can detect 100% of the BBH mergers with $\text{SNR} \geq 12$ up to $z = 1$. From our results, we find that up to $z = 0.23$, unique host associations are possible, i.e., $f_{\text{host}} \approx 1$. Together, this implies that the entire population of BBH mergers and their associated hosts

are detectable and potentially identifiable up to $z = 0.23$ in the 3G era. The event rate of BBH mergers with identifiable unique hosts per year is then

$$\mathcal{R}_{\text{host}} = \mathcal{R}_{\text{BBH}}(z) V_c(z) \mathcal{D} f_{\text{host}}, \quad (11)$$

where \mathcal{R}_{BBH} is the volumetric BBH merger rate. BBH merger rates are highly uncertain (see Mandel & Broekgaarden 2022 and Arca Sedda et al. 2023 for a review). LVK inferred the local ($z \approx 0$) BBH merger rate to be $14 - 26 \text{ Gpc}^{-3} \text{ yr}^{-1}$ (Abac et al. 2025c). Isolated BBH formation channels suggest a volumetric rate of $\mathcal{R}_{\text{BBH}} \sim 0.5 - 5 \times 10^3 \text{ Gpc}^{-3} \text{ yr}^{-1}$ at $z \lesssim 1$, while dynamical formation channels suggest $\mathcal{R}_{\text{BBH}} \sim 10^{-3} - 10^2 \text{ Gpc}^{-3} \text{ yr}^{-1}$ at similar redshifts (Mandel & Broekgaarden 2022; Arca Sedda et al. 2023). Here, we assume $\mathcal{R}_{\text{BBH}} \sim 50 \text{ Gpc}^{-3} \text{ yr}^{-1}$ at $z \lesssim 0.23$. V_c is the comoving volume, and at $z = 0.23$, $V_c = 3.45 \text{ Gpc}^3$. $\mathcal{D} = 0.85$ is the assumed duty cycle for ET in 1 year (Abac et al. 2025a). Under these assumptions, the expected number of BBH mergers with $\text{SNR} \geq 12$ with a uniquely identifiable host detected by ET alone is $\mathcal{R}_{\text{host}} \sim 100 \text{ yr}^{-1}$ at $z \lesssim 0.23$, consistent with estimates presented in figure 18 of Branchesi et al. (2023) and figure 2 of Gupta et al. (2024b).

5.2.6 Dependence on Host Galaxy Mass

We emphasize that this work was done under the assumption of a BBH merger occurring in a M_* galaxy. If instead we simulated the BBH mergers in lower mass galaxies (e.g. $10^8 M_\odot$), the corresponding V_{min} values would be $\approx 10^2 \text{ Mpc}^3$ for the distances considered here (Figure 4). The localization volumes achieved by the HLVKIEC and EC detector networks remain well below this threshold (Figures 5 and 8), indicating that unique host identification would still be feasible, even for dwarf-galaxy hosts.

5.3 Special Cases

In addition to the bulk of the BBH population which we might expect to form through standard binary evolution channels and hence to arise in otherwise normal galaxies, there are additional special cases that may arise in which the properties of the environment may be sufficiently unusual that they can be identified, even in larger uncertainty regions. These are the formation of BBH systems in AGN accretion discs, and cases in which the GW emission itself is lensed. A full consideration of these scenarios is beyond the scope of this paper, in principle the volumetric densities of both AGN and lensing systems are much lower than that of galaxies, such that such identifications should be more straightforward. We briefly consider each in turn.

In the case of BBH mergers formed through gas capture in AGN accretion discs (e.g. McKernan et al. 2020), we would expect to observe a clear AGN within the volumetric error boxes. Even in large current generation error boxes some claims have been made for AGN association based outbursts observed in the months after a BBH merger (Graham et al. 2020), although such claims are controversial. However, as error boxes get smaller, the probability of observing an AGN goes down. Even with 2G detectors it should be possible to identify AGN in some cases (Bartos et al. 2017). The minimum volume estimates for a AGN scenario in the 3G case will depend on assumptions about BBH formation rate as a function of AGN luminosity. However, even for faint AGN they are likely to be larger $\sim 1000 \text{ Mpc}^3$, suggesting that such associations will be straightforward for both EC and HLVKIEC configurations.

Similarly, the identification of lensed GW signals of significant

interest for a raft of scientific questions (see e.g., [Smith et al. 2025](#)). Ideally, such a lensing detection would consist of multiple detections of the same GW signal with variable magnification. However, Malmquist-bias may mean that it is sometimes only the most highly magnified events that are detected. The time delay between signals depends on the lensing mass and geometry. Large galaxy or cluster size lensing should be readily apparent in error boxes from EC or HLVKIEC configurations. Smaller scale lensing (shorter time delays) may not be, especially in cases where the angular separation of the multiple images is not resolved in existing imaging (i.e. where one cannot visually identify the lens). Nonetheless, the identification of lensing systems based on EM observations only, with no multiple GW detections at the time, may provide a route to enhancing the lensing return, in particular if these observations provide a route of searching for additional lensed signatures at lower SNRs.

6 CONCLUSION

As of March 2025, the LVK collaboration has reported ~ 210 detections of BBH mergers ($p_{\text{astro}} \geq 0.5$; [Abac et al. 2025c](#)), since the first GW detection of a BBH merger in 2015. The lack of EM emission from BBH mergers, combined with the large GW localization areas produced by the current-generation detector networks, makes the identification of a host to a BBH merger difficult. A confident host association would have several important astrophysical and cosmological implications, such as constraining BBH formation channels and providing an independent H_0 estimate. The planned addition of LIGO-India ([Unnikrishnan 2013, 2023; Shukla et al. 2024](#)) and 3G detectors such as ET ([Punturo et al. 2010; Hild et al. 2011; Maggiore et al. 2020; Abac et al. 2025a](#)) and CE ([Reitze et al. 2019; Evans et al. 2021, 2023](#)) is expected to reduce GW sky localization areas and improve distance precision for nearby, high-SNR events.

In this work, we simulate BBH mergers injected into M_* galaxies to assess the feasibility of such a host identification with future GW detector networks. We construct two complementary grids of injections: Grid I explores how localization performance scales with source properties such as mass and distance, while Grid II incorporates directional sensitivity through antenna patterns to evaluate sky-position dependence. We evaluate the inferred GW localization volumes from each injection using the FIM formalism as implemented within the BILBY framework, for three detector networks - HLV, HLVKIEC, and EC - and compare them to theoretical comoving volume thresholds derived from the GSMF, including thresholds computed using GSMFs weighted by assumptions about BBH formation via isolated binary evolution and dynamical assembly in dense stellar environments such as GCs.

To assess the implications for host identification and constraining the BBH formation channels, we introduce several diagnostics: (i) statistical volume thresholds ($V_{\min}^{\text{iso}}, V_{\min}^{\text{dyn}}$) corresponding to different BBH formation channels, (ii) a representative metallicity threshold motivated by progenitor environment constraints (V_{\min}^Z), (iii) the prominence of the injected host within the localization volume via mass fractions ($\mathbb{M}_{*,\Phi}$ and $\mathbb{M}_{*,\text{obs}}$), and (iv) the probability of chance alignment (p_c).

We find that 3G detector networks such as EC and HLVKIEC enable significant improvement in localization, achieving localisation volumes smaller than the theoretical thresholds for distances up to ~ 1000 Mpc. Under these conditions, unique host associations become feasible, at a rate of $\sim 100 \text{ yr}^{-1}$. Additionally, sub-threshold volumes enable statistical differentiation between isolated and dynamical BBH formation channels in favourable cases.

Future extensions of this work could include expanding the injection grid to consider galaxies of different stellar masses, out to higher redshifts ($z \sim 2$), and sampling a broader range of GW source parameters, such as mass fraction, spin, inclination, and eccentricity (Appendix A); incorporating models of galaxy catalogue completeness and selection effects; and applying the proposed metrics to real GW detections to evaluate candidate host associations. Additional BBH formation channels such as chemically homogeneous evolution, mergers in the accretion disks of AGNs, and hierarchical mergers, as well as mixed-channel scenarios involving multiple pathways within a single HG, also merit further investigation.

ACKNOWLEDGEMENTS

We are thankful to Christopher Berry for his useful comments on our draft. SB acknowledges studentship support from the Dutch Research Council (NWO) under the project number 680.92.18.02. PGJ is supported by the European Union (ERC, StarStruck, 101095973). Views and opinions expressed are however those of the author(s) only and do not necessarily reflect those of the European Union or the European Research Council. Neither the European Union nor the granting authority can be held responsible for them. This work made use of Python packages NUMPY ([Harris et al. 2020](#)), SCIPY ([Virtanen et al. 2020](#)), and MATPLOTLIB ([Hunter 2007](#)). This work made use of ASTROPY: a community-developed core Python package and an ecosystem of tools and resources for astronomy ([Astropy Collaboration et al. 2013, 2018, 2022](#)). The authors are grateful for computational resources provided by the LIGO Laboratory and supported by National Science Foundation Grants PHY-0757058 and PHY-0823459.

DATA AVAILABILITY

Relevant data and code will be made available in a reproduction package uploaded to Github at the following URL: <https://github.com/sumedhabiswas/popnet>.

REFERENCES

- Abac A., et al., 2025a, arXiv e-prints, p. arXiv:2503.12263
- Abac A. G., et al., 2025b, arXiv e-prints, p. arXiv:2508.18082
- Abac A. G., et al., 2025c, arXiv e-prints, p. arXiv:2508.18082
- Abac A. G., et al., 2025d, arXiv e-prints, p. arXiv:2509.04348
- Abbott B. P., et al., 2009, *Reports on Progress in Physics*, 72, 076901
- Abbott B. P., et al., 2016, *Phys. Rev. Lett.*, 116, 131103
- Abbott B., et al., 2017, *Physical Review Letters*, 119
- Abbott B. P., et al., 2018, *Living Reviews in Relativity*, 21, 3
- Abbott B. P., et al., 2019, *Physical Review X*, 9, 031040
- Abbott B. P., et al., 2020a, *Living Reviews in Relativity*, 23
- Abbott R., et al., 2020b, *Phys. Rev. Lett.*, 125, 101102
- Abbott R., et al., 2021a, *Physical Review X*, 11, 021053
- Abbott R., et al., 2021b, *The Astrophysical Journal Letters*, 915, L5
- Abbott R., et al., 2023a, *Physical Review X*, 13, 011048
- Abbott R., et al., 2023b, *Physical Review X*, 13, 041039
- Abbott R., et al., 2024, *Phys. Rev. D*, 109, 022001
- Acernese F., et al., 2014, *Classical and Quantum Gravity*, 32, 024001
- Acernese F., et al., 2019, *Phys. Rev. Lett.*, 123, 231108
- Acernese F., et al., 2023, *Classical and Quantum Gravity*, 40, 185006
- Ackermann M., et al., 2016, *ApJ*, 823, L2
- Akutsu T., et al., 2020, *Progress of Theoretical and Experimental Physics*, 2021, 05A101
- Amaro-Seoane P., et al., 2017, arXiv e-prints, p. arXiv:1702.00786

Andreoni I., et al., 2017, *Publ. Astron. Soc. Australia*, 34, e069

Antonini F., Toonen S., Hamers A. S., 2017, *ApJ*, 841, 77

Antonini F., Gieles M., Gualandris A., 2019, *MNRAS*, 486, 5008

Arca Sedda, Manuel Li, Gongjie Kocsis, Bence 2021, *A&A*, 650, A189

Arca Sedda M., Mapelli M., Spera M., Benacquista M., Giacobbo N., 2020, *ApJ*, 894, 133

Arca Sedda M., Naoz S., Kocsis B., 2023, *Universe*, 9, 138

Arcavi I., et al., 2017, *Nature*, 551, 64

Ashton G., et al., 2019, *The Astrophysical Journal Supplement Series*, 241, 27

Askar A., Szkudlarek M., Gondek-Rosińska D., Giersz M., Bulik T., 2017, *MNRAS*, 464, L36

Aso Y., Michimura Y., Somiya K., Ando M., Miyakawa O., Sekiguchi T., Tatsumi D., Yamamoto H., 2013, *Phys. Rev. D*, 88, 043007

Astropy Collaboration et al., 2013, *A&A*, 558, A33

Astropy Collaboration et al., 2018, *AJ*, 156, 123

Astropy Collaboration et al., 2022, *ApJ*, 935, 167

Baldry I. K., et al., 2012, *MNRAS*, 421, 621

Banerjee S., 2017, *MNRAS*, 467, 524

Banerjee S., Baumgardt H., Kroupa P., 2010, *MNRAS*, 402, 371

Barber J., Antonini F., 2025, *Monthly Notices of the Royal Astronomical Society*, 538, 639

Bartos I., Haiman Z., Marka Z., Metzger B. D., Stone N. C., Marka S., 2017, *Nature Communications*, 8, 831

Bavera S. S., et al., 2021, *A&A*, 647, A153

Belczynski K., et al., 2020, *A&A*, 636, A104

Belczynski K., Kalogera V., Bulik T., 2002, *ApJ*, 572, 407

Belczynski K., Kalogera V., Rasio F. A., Taam R. E., Zezas A., Bulik T., Maccarone T. J., Ivanova N., 2008, *ApJS*, 174, 223

Belczynski K., Dominik M., Bulik T., O’Shaughnessy R., Fryer C., Holz D. E., 2010, *ApJ*, 715, L138

Belczynski K., Holz D. E., Bulik T., O’Shaughnessy R., 2016, *Nature*, 534, 512–515

Bethe H. A., Brown G. E., 1998, *The Astrophysical Journal*, 506, 780

Biswas S., Jonker P. G., Miller M. C., Levan A., Quirola-Vásquez J., 2025, Comparing the Space Densities of Millisecond-Spin Magnetars and Fast X-Ray Transients ([arXiv:2506.11676](https://arxiv.org/abs/2506.11676)), <https://arxiv.org/abs/2506.11676>

Bloom J. S., Kulkarni S. R., Djorgovski S. G., 2002, *AJ*, 123, 1111

Bom C. R., Alfradique V., Palmese A., Teixeira G., Santana-Silva L., Santos A., Darc P., 2024, *MNRAS*, 535, 961

Borhanian S., Sathyaprakash B. S., 2024, *Phys. Rev. D*, 110, 083040

Bouffanais Y., Mapelli M., Santoliquido F., Giacobbo N., Di Carlo U. N., Rastello S., Artale M. C., Iorio G., 2021, *MNRAS*, 507, 5224

Branchesi M., et al., 2023, *Journal of Cosmology and Astroparticle Physics*, 2023, 068

Breivik K., Rodriguez C. L., Larson S. L., Kalogera V., Rasio F. A., 2016, *ApJ*, 830, L18

Cantiello M., et al., 2018, *ApJ*, 854, L31

Capote E., et al., 2025, *Phys. Rev. D*, 111, 062002

Chen H.-Y., Holz D. E., 2016, *arXiv e-prints*, p. [arXiv:1612.01471](https://arxiv.org/abs/1612.01471)

Choksi N., Volonteri M., Colpi M., Gnedin O. Y., Li H., 2019, *ApJ*, 873, 100

Chornock R., et al., 2017, *ApJ*, 848, L19

Colloms S., Berry C. P. L., Veitch J., Zevin M., 2025, *ApJ*, 988, 189

Colpi M., et al., 2024, *arXiv e-prints*, p. [arXiv:2402.07571](https://arxiv.org/abs/2402.07571)

Connaughton V., et al., 2016, *ApJ*, 826, L6

Connaughton V., et al., 2018, *ApJ*, 853, L9

Cook D. O., et al., 2023, *ApJS*, 268, 14

Coulter D. A., et al., 2017, *Science*, 358, 1556

Covino S., et al., 2017, *Nature Astron.*, 1, 791

Cowperthwaite P. S., et al., 2017, *ApJ*, 848, L17

Cutler C., Flanagan É. E., 1994, *Phys. Rev. D*, 49, 2658

Dall’Amico, Marco Mapelli, Michela Torniamenti, Stefano Arca Sedda, Manuel 2024, *A&A*, 683, A186

Davies M. B., Levan A. J., King A. R., 2005, *MNRAS*, 356, 54

Del Pozzo W., 2012, *Phys. Rev. D*, 86, 043011

Dodelson S., Hui L., Jaffe A., 1997, Likelihood Analysis of Galaxy Surveys ([arXiv:astro-ph/9712074](https://arxiv.org/abs/astro-ph/9712074)), <https://arxiv.org/abs/astro-ph/9712074>

Drout M. R., et al., 2017, *Science*, 358, 1570

Dvorkin I., Vangioni E., Silk J., Uzan J.-P., Olive K. A., 2016, *Monthly Notices of the Royal Astronomical Society*, 461, 3877

Dvorkin I., Uzan J.-P., Vangioni E., Silk J., 2018, *MNRAS*, 479, 121

Ebrová I., Bílek M., Yıldız M. K., Eliášek J., 2020, *A&A*, 634, A73

Eichler D., Livio M., Piran T., Schramm D. N., 1989, *Nature*, 340, 126

Eldridge J. J., Stanway E. R., 2016, *Monthly Notices of the Royal Astronomical Society*, 462, 3302

Evans P. A., et al., 2017, *Science*, 358, 1565

Evans M., et al., 2021, *arXiv e-prints*, p. [arXiv:2109.09882](https://arxiv.org/abs/2109.09882)

Evans M., et al., 2023, *arXiv e-prints*, p. [arXiv:2306.13745](https://arxiv.org/abs/2306.13745)

Ewing B., Sachdev S., Borhanian S., Sathyaprakash B. S., 2021, *Phys. Rev. D*, 103, 023025

Finn L. S., 2001, *Phys. Rev. D*, 63, 102001

Foucart F., et al., 2013, *Phys. Rev. D*, 87, 084006

Fragione G., Kocsis B., 2018, *Phys. Rev. Lett.*, 121, 161103

Fragione G., Kocsis B., 2019, *Monthly Notices of the Royal Astronomical Society*, 486, 4781

Fragione G., Loeb A., Rasio F. A., 2020, *The Astrophysical Journal Letters*, 902, L26

Gallegos-Garcia M., Berry C. P. L., Marchant P., Kalogera V., 2021, *The Astrophysical Journal*, 922, 110

Gehrels N., Cannizzo J. K., Kanner J., Kasliwal M. M., Nissanke S., Singer L. P., 2016, *The Astrophysical Journal*, 820, 136

Ghosh T., More S., Bera S., Bose S., 2024, in 32nd General Assembly International Union (IAUGA 2024). p. 1303 ([arXiv:2312.16305](https://arxiv.org/abs/2312.16305)), doi:10.48550/arXiv.2312.16305

Giacobbo N., Mapelli M., Spera M., 2018, *MNRAS*, 474, 2959

Gondán L., Kocsis B., Raffai P., Frei Z., 2018, *The Astrophysical Journal*, 855, 34

Górski K. M., Hivon E., Banday A. J., Wandelt B. D., Hansen F. K., Reinecke M., Bartelmann M., 2005, *ApJ*, 622, 759

Graham J. F., Fruchter A. S., 2017, *ApJ*, 834, 170

Graham M. J., et al., 2020, *Phys. Rev. Lett.*, 124, 251102

Gray R., Messenger C., Veitch J., 2022, *MNRAS*, 512, 1127

Gupta I., Borhanian S., Dhani A., Chattopadhyay D., Kashyap R., Villar V. A., Sathyaprakash B. S., 2023, *Phys. Rev. D*, 107, 124007

Gupta I., et al., 2024b, *Classical and Quantum Gravity*, 41, 245001

Gupta I., et al., 2024a, *Classical and Quantum Gravity*, 41, 245001

Hamers A. S., Safarzadeh M., 2020, *The Astrophysical Journal*, 898, 99

Harris W. E., Harris G. L. H., Alessi M., 2013, *ApJ*, 772, 82

Harris W. E., et al., 2014, *ApJ*, 797, 128

Harris C. R., et al., 2020, *Nature*, 585, 357

Hild S., et al., 2011, *Classical and Quantum Gravity*, 28, 094013

Hjorth J., et al., 2017, *ApJ*, 848, L31

Hong J., Vesperini E., Askar A., Giersz M., Szkudlarek M., Bulik T., 2018, *Monthly Notices of the Royal Astronomical Society*, 480, 5645

Howell E. J., et al., 2018, *MNRAS*, 474, 4385

Hunter J. D., 2007, *Computing in Science & Engineering*, 9, 90

Iacobelli F., Mancarella M., Foffa S., Maggiore M., 2022, *ApJ*, 941, 208

Im M., et al., 2017, *The Astrophysical Journal Letters*, 849, L16

Janiuk A., Bejger M., Charzyński S., Sukova P., 2017, *New Astron.*, 51, 7

Kagra Collaboration et al., 2019, *Nature Astronomy*, 3, 35

Kasliwal M. M., et al., 2017, *Science*, 358, 1559

Kilpatrick C. D., et al., 2022, *The Astrophysical Journal*, 926, 49

Kinugawa T., Nakamura T., Nakano H., 2024, *Monthly Notices of the Royal Astronomical Society*, 531, 4725

Klencki, Jakub Nelemans, Gijs Istrate, Alina G. Chruslinska, Martyna 2021, *A&A*, 645, A54

Kruckow M. U., Tauris T. M., Langer N., Kramer M., Izzard R. G., 2018, *MNRAS*, 481, 1908

Kumamoto J., Fujii M. S., Tanikawa A., 2020, *MNRAS*, 495, 4268

Lamberts A., Garrison-Kimmel S., Clausen D. R., Hopkins P. F., 2016, *MNRAS*, 463, L31

Levan A. J., et al., 2017, *ApJ*, 848, L28

Levan A. J., et al., 2024, *Nature*, 626, 737

Li L.-X., Paczyński B., 1998a, *ApJ*, **507**, L59

Li L.-X., Paczyński B., 1998b, *ApJ*, **507**, L59

Lin D., Irwin J. A., Berger E., Nguyen R., 2022, *The Astrophysical Journal*, **927**, 211

Lipunov V. M., et al., 2017, *ApJ*, **850**, L1

Ma S., Cao Z., Lin C.-Y., Pan H.-P., Yo H.-J., 2017, *Phys. Rev. D*, **96**, 084046

MacLeod C. L., Hogan C. J., 2008, *Phys. Rev. D*, **77**, 043512

Maggiore M., et al., 2020, *J. Cosmology Astropart. Phys.*, **2020**, 050

Mandel I., Broekgaarden F. S., 2022, *Living Reviews in Relativity*, **25**, 1

Mandel I., de Mink S. E., 2016, *Monthly Notices of the Royal Astronomical Society*, **458**, 2634

Mapelli M., 2016, *Monthly Notices of the Royal Astronomical Society*, **459**, 3432

Mapelli M., 2020, *Formation Channels of Single and Binary Stellar-Mass Black Holes*. Springer Singapore, Singapore, pp 1–65, doi:10.1007/978-981-15-4702-7_16-1, https://doi.org/10.1007/978-981-15-4702-7_16-1

Mapelli M., Giacobbo N., Ripamonti E., Spera M., 2017, *Monthly Notices of the Royal Astronomical Society*, **472**, 2422

Mapelli M., Giacobbo N., Santoliquido F., Artale M. C., 2019, *MNRAS*, **487**, 2

Mapelli M., Bouffanais Y., Santoliquido F., Arca Sedda M., Artale M. C., 2022, *MNRAS*, **511**, 5797

Marchant P., Langer N., Podsiadlowski P., Tauris T. M., Moriya T. J., 2016, *A&A*, **588**, A50

Martinez M. A. S., et al., 2020, *ApJ*, **903**, 67

McKernan B., et al., 2019, *The Astrophysical Journal Letters*, **884**, L50

McKernan B., Ford K. E. S., O’Shaughnessy R., 2020, *MNRAS*, **498**, 4088

McLeod D. J., McLure R. J., Dunlop J. S., Cullen F., Carnall A. C., Duncan K., 2021, *Monthly Notices of the Royal Astronomical Society*, **503**, 4413

Messenger C., Takami K., Gossan S., Rezzolla L., Sathyaprakash B. S., 2014, *Phys. Rev. X*, **4**, 041004

Metzger B. D., Berger E., 2012, *The Astrophysical Journal*, **746**, 48

Mo G., Chen H.-Y., 2024, arXiv e-prints, p. arXiv:2402.09684

Moustakas J., et al., 2011, arXiv e-prints, p. arXiv:1112.3300

Narayan R., Paczynski B., Piran T., 1992, *ApJ*, **395**, L83

Neijssel C. J., et al., 2019, *MNRAS*, **490**, 3740

Nicholl M., et al., 2017, *ApJ*, **848**, L18

Nishizawa A., Berti E., Klein A., Sesana A., 2016, *Phys. Rev. D*, **94**, 064020

Nishizawa A., Sesana A., Berti E., Klein A., 2017, *MNRAS*, **465**, 4375

Nuttall L. K., Sutton P. J., 2010, *Phys. Rev. D*, **82**, 102002

Olejak A., Belczynski K., Ivanova N., 2021, *A&A*, **651**, A100

Palmese A., Fishbach M., Burke C. J., Annis J., Liu X., 2021, *The Astrophysical Journal Letters*, **914**, L34

Pan H.-P., Lin C.-Y., Cao Z., Yo H.-J., 2019, *Phys. Rev. D*, **100**, 124003

Pankow C., Rizzo M., Rao K., Berry C. P. L., Kalogera V., 2020, *ApJ*, **902**, 71

Parzen E., 1962, *The Annals of Mathematical Statistics*, **33**, 1065

Perna R., Lazzati D., Giacomazzo B., 2016, *The Astrophysical Journal Letters*, **821**, L18

Peters P. C., 1964, *Phys. Rev.*, **136**, B1224

Pian E., et al., 2017, *Nature*, **551**, 67

Portegies Zwart S. F., McMillan S. L. W., 2000, *ApJ*, **528**, L17

Portegies Zwart S. F., Yungelson L. R., 1998, *A&A*, **332**, 173

Pratten G., et al., 2021, *Physical Review D*, **103**

Punturo M., et al., 2010, *Classical and Quantum Gravity*, **27**, 194002

Quirola-Vásquez J., et al., 2024, *A&A*, **683**, A243

Rastinejad J. C., et al., 2022, *Nature*, **612**, 223

Reitze D., et al., 2019, in *Bulletin of the American Astronomical Society*, p. 35 (arXiv:1907.04833), doi:10.48550/arXiv.1907.04833

Riley J., Mandel I., Marchant P., Butler E., Nathaniel K., Neijssel C., Shortt S., Vigna-Gómez A., 2021, *MNRAS*, **505**, 663

Rodriguez C. L., Chatterjee S., Rasio F. A., 2016, *Phys. Rev. D*, **93**, 084029

Rosenblatt M., 1956, *The Annals of Mathematical Statistics*, **27**, 832

Samsing J., MacLeod M., Ramirez-Ruiz E., 2014, *ApJ*, **784**, 71

Santoliquido F., Mapelli M., Artale M. C., Boco L., 2022, *MNRAS*, **516**, 3297

Savchenko V., et al., 2016, *The Astrophysical Journal Letters*, **820**, L36

Schechter P., 1976, *ApJ*, **203**, 297

Schutz B. F., 2011, *Classical and Quantum Gravity*, **28**, 125023

Shao Y., Li X.-D., 2021, *The Astrophysical Journal*, **920**, 81

Shappee B. J., et al., 2017, *Science*, **358**, 1574

Shukla S. R., Pathak L., Sengupta A. S., 2024, *Phys. Rev. D*, **109**, 044051

Siegel D. M., Ciolfi R., 2016a, *ApJ*, **819**, 14

Siegel D. M., Ciolfi R., 2016b, *The Astrophysical Journal*, **819**, 15

Silsbee K., Tremaine S., 2017, *The Astrophysical Journal*, **836**, 39

Smartt S. J., et al., 2017b, *Nature*, **551**, 75

Smartt S. J., et al., 2017a, *Nature*, **551**, 75

Smith G. P., et al., 2025, *Philosophical Transactions of the Royal Society of London Series A*, **383**, 20240134

Soares-Santos M., et al., 2017, *The Astrophysical Journal Letters*, **848**, L16

Speagle J. S., 2020, *MNRAS*, **493**, 3132

Spera M., Mapelli M., Giacobbo N., Trani A. A., Bressan A., Costa G., 2019, *Monthly Notices of the Royal Astronomical Society*, **485**, 889–907

Stevenson S., Berry C. P. L., Mandel I., 2017, *Monthly Notices of the Royal Astronomical Society*, **471**, 2801

Sun B., Cao Z., Wang Y., Yeh H.-C., 2015, *Phys. Rev. D*, **92**, 044034

Sun H., Zhang B., Gao H., 2017, in Ness J.-U., Migliari S., eds, *The X-ray Universe 2017*. p. 216

Sun H., Li Y., Zhang B.-B., Zhang B., Bauer F. E., Xue Y., Yuan W., 2019, *ApJ*, **886**, 129

Sun H., et al., 2024, *National Science Review*, **12**, nwae401

Tanikawa A., 2013, *MNRAS*, **435**, 1358

Tanikawa A., Kinugawa T., Yoshida T., Hijikawa K., Umeda H., 2021, *Monthly Notices of the Royal Astronomical Society*, **505**, 2170

Tanvir N. R., Levan A. J., Fruchter A. S., Hjorth J., Hounsell R. A., Wiersema K., Tunnicliffe R. L., 2013, *Nature*, **500**, 547

Tanvir N. R., et al., 2017a, *The Astrophysical Journal*, **848**, L27

Tanvir N. R., et al., 2017b, *ApJ*, **848**, L27

Tremonti C. A., et al., 2004, *ApJ*, **613**, 898

Troja E., et al., 2017, *Nature*, **551**, 71

Troja E., et al., 2022, *Nature*, **612**, 228

Unnikrishnan C. S., 2013, *International Journal of Modern Physics D*, **22**, 1341010

Unnikrishnan C. S., 2023, arXiv e-prints, p. arXiv:2301.07522

Utsumi Y., et al., 2017, *Publications of the Astronomical Society of Japan*, **69**

Vallisneri M., 2008, *Phys. Rev. D*, **77**, 042001

Veronesi N., van Velzen S., Rossi E. M., 2025, *MNRAS*, **536**, 3112

Virtanen P., et al., 2020, *Nature Methods*, **17**, 261

Weigel A. K., Schwabinski K., Bruderer C., 2016, *MNRAS*, **459**, 2150

Yang S., et al., 2019, *The Astrophysical Journal*, **875**, 59

Yang T., Cai R.-G., Cao Z., Lee H. M., 2024, *Phys. Rev. D*, **109**, 104041

Ye C. S., Kremer K., Rodriguez C. L., Rui N. Z., Weatherford N. C., Chatterjee S., Fragione G., Rasio F. A., 2022, *ApJ*, **931**, 84

Zahid H. J., Dima G. I., Kudritzki R.-P., Kewley L. J., Geller M. J., Hwang H. S., Silverman J. D., Kashino D., 2014, *ApJ*, **791**, 130

Zaritsky D., et al., 2015, *ApJ*, **799**, 159

Zevin M., Romero-Shaw I. M., Kremer K., Thrane E., Lasky P. D., 2021, *ApJ*, **921**, L43

de Mink S. E., Mandel I., 2016, *MNRAS*, **460**, 3545

du Buisson L., et al., 2020, *MNRAS*, **499**, 5941

APPENDIX A: DEPENDENCE OF GW LOCALIZATION ON SOURCE PARAMETERS AND CONSISTENCY WITH GW OBSERVATIONS

In our BILBY simulations, BBH mergers are modelled using fixed GW source parameters, as summarized in Tables 4 and 5. This subsection evaluates how these modelling assumptions influence our analysis outcomes and compares the chosen parameter values to those inferred from observed GW events. As an example, Figure A1 shows the 2D localization areas of a 50+50 M_⊙ Grid I injection at 1000 Mpc.

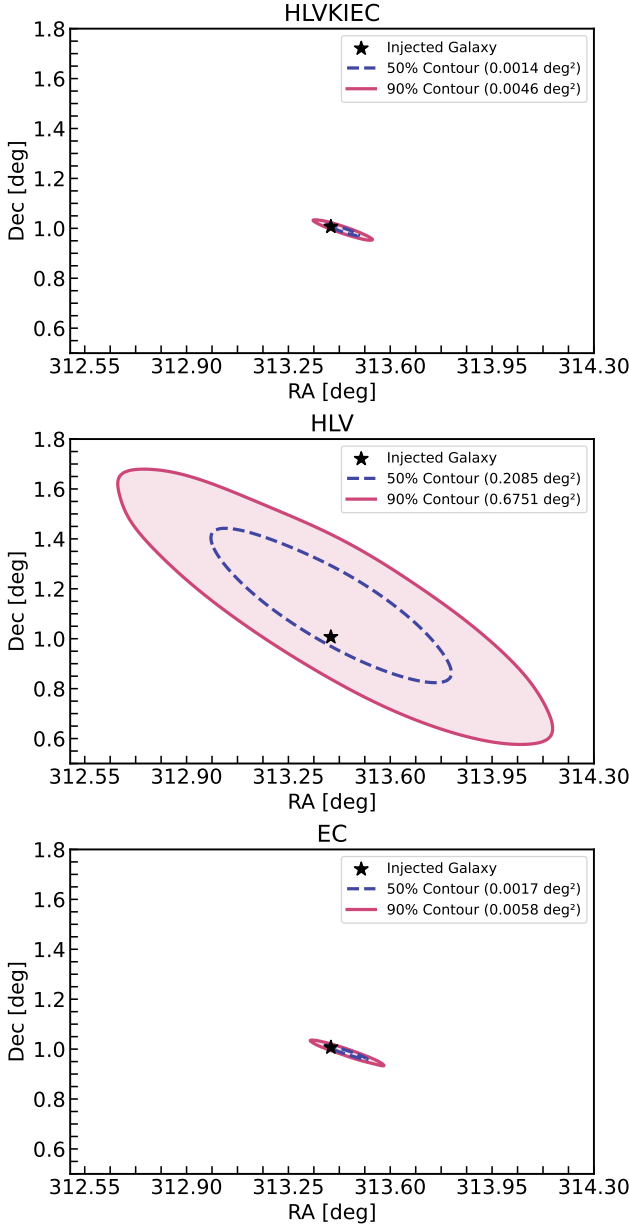


Figure A1. Skymaps for the $50+50 M_{\odot}$ injection at 1000 Mpc ($\text{RA} = 313.4^{\circ}$, $\text{Dec} = 1.0^{\circ}$; black star), as recovered by the 3 detector networks: HLVKIEC (top), HLV (middle), and EC (bottom). Each panel shows the 50% (dashed indigo) and 90% (solid magenta) regions.

A1 Eccentricity

Eccentricity is an important parameter, both for distinguishing BBH formation channels (e.g. [Nishizawa et al. 2016, 2017](#); [Breivik et al. 2016](#); [Zevin et al. 2021](#)) and understanding its impact on GW localization regions (e.g. [Sun et al. 2015](#); [Ma et al. 2017](#); [Yang et al. 2024](#)). Dynamical channels, such as those involving GCs or hierarchical triples, can retain measurable eccentricity by the time the binary enters the ground-based GW detector band, especially at lower GW frequencies (e.g. [Dall’Amico, Marco et al. 2024](#)). In contrast, BBHs formed through isolated binary evolution are expected to cir-

cularize efficiently via gravitational radiation, making the assumption of quasi-circular orbits well justified in that scenario ([Peters 1964](#)). In our simulations, we use the `IMRPhenomXPHM` waveform approximant ([Pratten et al. 2021](#)), which assumes quasi-circular (i.e., non-eccentric) binaries. While this is appropriate for the isolated channel, previous studies have shown that even moderate eccentricity can improve localization performance. [Ma et al. \(2017\)](#) find that increasing the eccentricity from 0 to 0.4 improves localization by a factor of ~ 2 for a binary with a total mass of $100 M_{\odot}$, and by a factor of ~ 1.3 for a GW150914-like system (total mass of $65 M_{\odot}$; [Abbott et al. 2024](#)). For lower-mass binaries such as GW151226 (total mass of $22 M_{\odot}$; [Abbott et al. 2024](#)), the improvement is negligible. [Gondán et al. \(2018\)](#) report similar trends: for a $30+30 M_{\odot}$ non-spinning BBH with high eccentricity (pericenter distance of $20 M_{\text{tot}}$), localization improves by a factor of ~ 2 . [Pan et al. \(2019\)](#) also demonstrated that the accuracy of sky localization increases appreciably with eccentricity for binaries with total mass $M \geq 40 M_{\odot}$, while the effect is negligible for lower-mass systems. These findings suggest that our localization estimates for dynamically formed BBHs, particularly at higher masses, may represent conservative lower limits, as the inclusion of eccentricity would likely enhance localization performance beyond what is captured in our quasi-circular simulations. Consequently, for dynamically formed BBHs with non-negligible eccentricity, incorporating eccentric waveforms in future analyses may not only improve localization accuracy but also increase the likelihood of successful host identification.

A2 Mass Ratio (q)

In our injections, we adopt equal-mass binaries with primary and secondary BH masses drawn from the set $[50.0, 40.0, 30.0, 20.0, 10.0, 5.0] M_{\odot}$, resulting in a fixed mass ratio of $q = 1$ across all injections. This choice is observationally motivated: analyses of the GWTC-3.0 catalogue ([Abbott et al. 2023a,b](#)) suggest that BBH systems with symmetric mass ratios $q \gtrsim 0.7$ dominate the population, particularly among high-mass mergers ([Kinugawa et al. 2024](#)). As such, our adopted mass ratio represents a physically plausible configuration within the observed BBH population. For further context, in Figure 11, we calculate and plot the source-frame chirp masses⁵ $\mathcal{M}_c = (m_1 m_2)^{3/5} / (m_1 + m_2)^{1/5}$ of our equal-mass injections as a function of redshift, and compare them to GW observations (GWTC-4.0; [Abbott et al. 2019, 2021a, 2024, 2023b](#); [Abac et al. 2025c](#)).

A3 BH Spins (a_1, a_2)

In our injections, we fix the dimensionless spin magnitudes of both BHs to $a_1 = a_2 = 0.1$, corresponding to nearly non-spinning BHs. This is motivated by population-level analyses of the GWTC-3.0 catalog ([Abbott et al. 2023b](#)), which suggest that low spin magnitudes are preferentially associated with symmetric mass-ratio binaries ($q = 1$) ([Abbott et al. 2023a](#)) (see their figure 21). Our adopted spin and mass ratio values are therefore broadly consistent with current observational constraints.

⁵ The error bars on chirp mass are accurate to $\sim 0.1\text{--}1\%$ ([Cutler & Flanagan 1994](#)), dependent on the waveform model, and degenerate with spin and the $\mathcal{M}_c - z$ degeneracy ([Messenger et al. 2014](#)).

A4 Binary Inclination Angle (θ_{JN})

In all our injections, we fix the binary inclination angle to $\theta_{\text{JN}} = 0.4$ radians, corresponding to a nearly face-on orientation. Such configurations yield GW signals with higher SNRs and tighter posterior distributions, leading to reduced localization volumes. Therefore, our choice of $\theta_{\text{JN}} = 0.4$ radians approximates a best-case scenario for source localization.

This paper has been typeset from a $\text{\TeX}/\text{\LaTeX}$ file prepared by the author.